

*On the momentum flux of vertically-propagating orographic gravity waves excited in nonhydrostatic flow over three-dimensional orography*

Article

Accepted Version

Xu, X., Li, R., Teixeira, M. A. C. ORCID: <https://orcid.org/0000-0003-1205-3233> and Lu, Y. (2021) On the momentum flux of vertically-propagating orographic gravity waves excited in nonhydrostatic flow over three-dimensional orography. *Journal of the Atmospheric Sciences*, 78 (6). pp. 1807-1822. ISSN 1520-0469 doi: 10.1175/JAS-D-20-0370.1 Available at <https://centaur.reading.ac.uk/97296/>

It is advisable to refer to the publisher's version if you intend to cite from the work. See [Guidance on citing](#).

To link to this article DOI: <http://dx.doi.org/10.1175/JAS-D-20-0370.1>

Publisher: American Meteorological Society

All outputs in CentAUR are protected by Intellectual Property Rights law, including copyright law. Copyright and IPR is retained by the creators or other copyright holders. Terms and conditions for use of this material are defined in the [End User Agreement](#).

[www.reading.ac.uk/centaur](http://www.reading.ac.uk/centaur)

**CentAUR**

Central Archive at the University of Reading

Reading's research outputs online

1  
2  
3  
4  
5  
6  
7  
8  
9  
10  
11  
12  
13  
14  
15  
16  
17  
18  
19  
20  
21  
22  
23  
24  
25  
26  
27  
28  
29  
30  
31

**On the Momentum Flux of Vertically-Propagating Orographic Gravity Waves  
Excited in Nonhydrostatic Flow over Three-dimensional Orography**

Xin Xu<sup>1</sup>, Runqiu Li<sup>1</sup>, Miguel A. C. Teixeira<sup>2</sup>, Yixiong Lu<sup>3</sup>

<sup>1</sup>*Key Laboratory of Mesoscale Severe Weather/Ministry of Education, and School of Atmospheric Sciences, Nanjing University, Nanjing 210023, Jiangsu, P. R. China*  
<sup>2</sup>*University of Reading, Department of Meteorology, Meteorology Building, Whiteknights Road, Earley Gate, Reading RG6 6ET, UK*  
<sup>3</sup>*Beijing Climate Center, China Meteorological Administration, Beijing 100081, P. R. China*

Submitted to *Journal of the Atmospheric Sciences*  
8th December 2020

Corresponding to: Xin Xu (xinxu@nju.edu.cn)  
School of Atmospheric Sciences, Nanjing University  
No. 163, Xianlin Avenue, Nanjing, Jiangsu, 210023, P. R. China

## Abstract

32  
33 This work studies nonhydrostatic effects (NHE) on the momentum flux of orographic  
34 gravity waves (OGWs) forced by isolated three-dimensional orography. Based on linear wave  
35 theory, an asymptotic expression for low horizontal Froude number ( $Fr = \frac{\sqrt{U^2 + (\gamma V)^2}}{Na}$  where  $(U, V)$   
36 is the mean horizontal wind,  $\gamma$  and  $a$  are the orography anisotropy and half-width and  $N$  is the  
37 buoyancy frequency) is derived for the gravity wave momentum flux (GWMF) of vertically-  
38 propagating waves. According to this asymptotic solution, which is quite accurate for any value of  
39  $Fr$ , NHE can be divided into two terms (NHE1 and NHE2). The first term contains the high-  
40 frequency parts of the wave spectrum that are often mistaken as hydrostatic waves, and only  
41 depends on  $Fr$ . The second term arises from the difference between the dispersion relationships of  
42 hydrostatic and nonhydrostatic OGWs. Having an additional dependency on the horizontal wind  
43 direction and orography anisotropy, this term can change the GWMF direction. Examination of  
44 NHE for OGWs forced by both circular and elliptical orography reveals that the GWMF is reduced  
45 as  $Fr$  increases, at a faster rate than for two-dimensional OGWs forced by a ridge. At low  $Fr$ , the  
46 GWMF reduction is mostly attributed to the NHE2 term, whereas the NHE1 term starts to  
47 dominate above about  $Fr = 0.4$ . The behavior of NHE is mainly determined by  $Fr$ , while horizontal  
48 wind direction and orography anisotropy play a minor role. Implications of the asymptotic GWMF  
49 expression for the parameterization of nonhydrostatic OGWs in high-resolution and/or variable-  
50 resolution models are discussed.

## 51 **1 Introduction**

52 Orographic gravity waves (OGWs) triggered by stably stratified airflow over topography  
53 have been the subject of many studies over the last century. These waves can propagate upward  
54 and thus have great importance for the large-scale circulation in the middle atmosphere (Fritts and  
55 Alexander 2003). They are also closely related to various severe weather phenomena, like clear  
56 air turbulence (CAT) and downslope windstorms occurring in the troposphere (Smith 1985). Given  
57 that their horizontal spatial scales vary from a few to hundreds of kilometers, OGWs cannot be  
58 fully resolved by numerical weather prediction (NWP) and general circulation models (GCMs).  
59 As a result, the impacts of unresolved OGWs need to be parameterized (Kim et al. 2003).

60 Many parameterization schemes have been developed for subgrid-scale OGWs since the  
61 1980s (e.g., Palmer et al. 1986; McFarlane 1987; Kim and Arakawa 1995; Lott and Miller 1997;  
62 Scinocca and MacFarlane 2000; Kim and Doyle 2005), which are now routinely implemented in  
63 various operational models for both weather forecasts and climate simulations. In general, these  
64 schemes share many common assumptions, such as the columnar propagation of OGWs  
65 (Plougonven et al. 2020). They also assume that OGWs are generated in a non-rotating and  
66 hydrostatic framework. A state-of-the-art NWP model, the Integrated Forecasting System (IFS)  
67 model of the European Centre for Medium-range Weather Forecasts (ECMWF), has horizontal  
68 resolutions typically on the order of 10 km. In these circumstances, the non-rotating assumption is  
69 justified because the subgrid-scale OGWs are too short to be affected by the earth's rotation.  
70 However, this is not the case with the assumption of hydrostatic OGWs.

71 For small-scale OGWs with horizontal wavenumber comparable to the Scorer parameter  
72 (Scorer 1949), nonhydrostatic effects (NHE) play a key role in controlling the wave dynamics.  
73 Using the stationary phase method, Smith (1979) theoretically studied the far-field OGWs excited

74 by a narrow two-dimensional (2D) ridge, which are nonhydrostatic. A “dispersive tail” was found  
75 to trail downstream of the mountain, which was also revealed in a number of numerical simulations  
76 (e.g., Klemp and Durran 1983; Xue and Thorpe 1991; Zängl 2003). This suggests that the wave  
77 energy can, not only propagate upwards as in the case of hydrostatic OGWs, but also disperse  
78 downstream. Owing to nonhydrostatic dispersion, the wave activity above the mountain is weaker  
79 than in its hydrostatic counterpart, leading to a suppression of wave breaking (Zängl 2003).  
80 Nonetheless, NHE on wave breaking can be modified by the interaction between OGWs and  
81 critical levels, as studied in Guarino and Teixeira (2017) for three-dimensional (3D) OGWs excited  
82 in directional shear flows past isolated mountains. These modeling results showed that wave  
83 breaking tends to be inhibited when the background shear is weak while it is enhanced for stronger  
84 wind shear. Besides wave breaking, NHE can also influence the gravity wave momentum flux  
85 (GWMF) at the surface. The high-frequency parts of nonhydrostatic OGWs (i.e., short-wavelength  
86 components) tend to be trapped in the lower troposphere (e.g., Wurtele et al. 1996; Doyle and  
87 Durran 2002). Consequently, the GWMF associated with upward-propagating waves is smaller  
88 than that existing in the hydrostatic case (e.g., Xue et al. 2000).

89         The GWMF at the surface is a key parameter in the parameterization schemes of OGWs.  
90 It denotes the maximum GWMF that can be absorbed into the mean flow. Changes in the surface  
91 GWMF can affect wave breaking at high altitudes (Xu et al. 2020) and thus redistribute the wave  
92 momentum deposition, impacting the large-scale circulation in the middle atmosphere (Xu et al.  
93 2019). However, NHE are not considered in any OGW parameterization scheme. This is mainly  
94 due to the fact that there is no analytical solution for nonhydrostatic OGWs except for very special  
95 cases. To compensate for this, some OGW parametrization schemes (e.g., Lott and Miller 1997)  
96 filter all orography of horizontal scale smaller than a few km out of the orography that serves as

97 input to the OGW parametrization, assuming that it only causes turbulent orographic form drag  
98 (TOFD) which is the object of a separate parametrization (e.g., Beljaars et al. 2004). However, this  
99 filtering procedure is somewhat arbitrary, ignoring the influence of the flow characteristics on how  
100 non-hydrostatic the OGWs are, and how reduced their GWMF is by NHE. In the present study,  
101 this limitation will be overcome.

102         Smith (1980) proposed solving the wave equation of nonhydrostatic OGWs numerically  
103 using the Fast Fourier Transform (FFT) technique, which is apparently not suitable for the purpose  
104 of OGW parameterization given its computational cost. Alternatively, ray theory has been widely  
105 adopted to obtain the asymptotic solutions of nonhydrostatic OGWs. For instance, Smith (1979)  
106 derived the far-field approximation of 2D nonhydrostatic OGWs, while Marks and Eckermann  
107 (1995) developed a ray-tracing model for 3D nonhydrostatic gravity waves in a rotating, stratified  
108 and fully compressible atmosphere. Standard ray theory often utilizes the stationary-phase method  
109 and the asymptotic solution is expressed in spatial coordinates (Shutts 1998). This spatial-ray  
110 solution is inaccurate directly over the mountain because of the presence of ray caustics there. To  
111 overcome this problem, Broutman et al. (2002) expressed the ray solution in the wavenumber  
112 rather than spatial domain, i.e., Maslov's method. This eliminates the caustics over the mountain  
113 because rays in the spectral domain are well separated. Broutman et al. (2003) further extended  
114 the so-called Fourier-ray solution to accommodate nonhydrostatic OGWs, which showed good  
115 agreement with numerical simulations. Nonetheless, the Fourier-ray solution also has caustics at  
116 the buoyancy-frequency turning point for nonhydrostatic waves. Later, Pulido and Rodas (2011)  
117 developed a higher-order ray approximation method, i.e., the Gaussian beam approximation  
118 (GBA), for OGWs generated in vertically sheared flows. In the standard ray theory, each ray only  
119 consists of a single monochromatic wavenumber (i.e., the characteristic wavenumber). On the

120 contrary, the GBA uses a bundle of rays centered at the characteristic wavenumber (i.e., Gaussian  
121 beams) for each ray, and considers diffractive effects. Therefore, the GBA solution is well defined  
122 even at caustics. However, all these studies focused on the wave fields rather than on the GWMF  
123 and hence OGW parameterization. Based on the GBA, Xu et al. (2017a, 2018) revised a traditional  
124 OGW parameterization scheme by explicitly incorporating the horizontal propagation (e.g.,  
125 Eckermann et al. 2015; Ehard et al. 2017) and directional absorption (e.g., Shutts 1995; Xu et al.  
126 2012; Teixeira and Miranda 2009; Teixeira and Yu 2014) of OGWs. The revised scheme was  
127 implemented into the global Weather Research and Forecasting (WRF) model, and helped improve  
128 the simulation of the stratospheric polar-night jet in the Northern Hemisphere (Xu et al. 2019).

129         Compared with the traditional parameterization schemes of OGWs, ray-tracing based  
130 schemes have to keep track of a number of rays, which requires a significant amount of  
131 computation (e.g., Song and Chun 2008; Amemiya and Sato 2016). This approach is thus not  
132 suitable for operational use. Teixeira et al. (2008, hereafter T08) studied the surface GWMF  
133 associated with vertically-propagating OGWs produced by nonhydrostatic and rotating flow over  
134 a 2D ridge. Instead of calculating the GWMF numerically, an asymptotic expression was derived  
135 by using Taylor expansion for weakly-nonhydrostatic and weakly-rotating conditions. Fortuitously,  
136 the asymptotic expansion was found to be fairly accurate even for nonhydrostatic inertio-gravity  
137 waves, i.e., when the nonhydrostatic or rotation effects were not weak. The analytical form of this  
138 asymptotic expression of GWMF makes it promising for practical use in OGW parameterizations  
139 in numerical models. However, T08 only considered 2D OGWs forced by a ridge, while subgrid-  
140 scale OGWs are intrinsically 3D (Lott and Miller 1997; Kim and Doyle 2005). In this work, an  
141 asymptotic expression will be derived for 3D GWMF to accommodate the parameterization of 3D

142 nonhydrostatic OGWs. This provides a physically-based, flow-dependent, alternative to simply  
143 filtering out the GWMF associated with waves shorter than a prescribed scale.

144 The rest of the paper is organized as follows. Section 2 presents the expression for surface  
145 GWMF of 3D nonhydrostatic OGWs from linear mountain wave theory. An asymptotic solution  
146 is derived in section 3 for the linear nonhydrostatic GWMF associated with vertically-propagating  
147 OGWs. The behavior of this GWMF solution is studied for both isotropic and elliptical mountains  
148 in section 4. Finally, the paper is summarized and discussed in section 5.

149

## 150 **2 Linear theory of nonhydrostatic OGWs**

151 In the case of steady, adiabatic, inviscid, and Boussinesq flow, the governing equation for  
152 the perturbed vertical velocity of gravity waves in spectral space is

$$153 \left. \frac{\partial^2 \hat{w}}{\partial z^2} + \left[ \frac{N^2 K^2}{\hat{D}(z)^2} - \frac{1}{\hat{D}(z)} \frac{\partial^2 \hat{D}(z)}{\partial z^2} - K^2 \right] \hat{w} = 0, \right. \quad (1)$$

154 where  $N$  is the Brunt-Väisälä frequency,  $K = \sqrt{k^2 + l^2}$  is the magnitude of horizontal  
155 wavenumber vector  $\mathbf{K} = (k, l)$ , and  $\hat{D}(z) = \mathbf{V}(z) \cdot \mathbf{K} = U(z)k + V(z)l$ , with  $\mathbf{V}(z)$  being a  
156 horizontally uniform mean flow. The above equation is similar to Eq. (9) in Xu et al. (2012) except  
157 for the last term  $K^2$  within the brackets, which denotes the NHE. The Earth's rotation is neglected  
158 because we only consider nonhydrostatic OGWs forced by relatively narrow orography.

159 In the parameterization schemes of OGWs, the mean flow is assumed to be constant when  
160 calculating the surface GWMF (e.g., Lott and Miller 1997), although vertical wind shear (either  
161 unidirectional or directional) definitely influences the GWMF (e.g., Grubišić et al. 1997; Teixeira  
162 et al. 2004; Turner et al. 2019; Xu et al. 2020). Herein, we also make this assumption, to be

163 consistent with existing parameterization schemes. For constant wind, i.e.,  $\mathbf{V}(z) = \mathbf{V}_0 =$   
 164  $(U_0, V_0)$ , Eq. (1) simplifies to

$$165 \quad \frac{\partial^2 \hat{w}}{\partial z^2} + m^2 \hat{w} = 0, \quad (2)$$

166 where  $m^2 = \frac{N^2 K^2}{\hat{D}_0^2} - K^2$  is the squared vertical wavenumber, and  $\hat{D}_0 = \mathbf{V}_0 \cdot \mathbf{K} = U_0 k + V_0 l =$   
 167  $|\mathbf{V}_0| K \cos(\varphi - \psi_0)$ , with  $\varphi$  and  $\psi_0$  being the directions of  $\mathbf{K}$  and  $\mathbf{V}_0$  respectively. For vertically-  
 168 propagating OGWs the magnitude of the horizontal wavenumber should be smaller than  
 169  $\left| \frac{N}{\mathbf{V}_0 \cos(\varphi - \psi_0)} \right|$ . Otherwise, the vertical wavenumber will be imaginary, indicating evanescent waves  
 170 that decay exponentially with height.

171 Under the free-slip condition at the bottom boundary, i.e.,  $w(z = 0) = \mathbf{V}_0 \cdot \nabla h(x, y)$ , the  
 172 vertical velocity of upward-propagating OGWs can be determined as

$$173 \quad \hat{w}(z) = i \hat{D}_0 \hat{h}(k, l) e^{imz}, \quad (3)$$

174 where  $\hat{h}(k, l)$  is the 2D Fourier transform of the terrain elevation  $h(x, y)$ . In idealized studies of  
 175 OGWs and their parameterizations (e.g., Phillips 1984; Lott and Miller 1997; Teixeira and  
 176 Miranda 2006), elliptical bell-shaped mountains are often adopted, a convenient example of which  
 177 is:

$$178 \quad h(x, y) = h_0 [1 + (x/a)^2 + (y/b)^2]^{-3/2}, \quad (4)$$

179 where  $h_0$  is the mountain amplitude, and  $a$  and  $b$  are the mountain half widths in the  $x$  and  $y$   
 180 directions, respectively. The horizontal aspect ratio (i.e., anisotropy) of the elliptical terrain is  
 181 quantified by  $\gamma = \frac{a}{b}$ . The 2D Fourier transform of the terrain elevation is given by

$$182 \quad \hat{h}(k, l) = \frac{h_0 ab}{2\pi} e^{-\sqrt{a^2 k^2 + b^2 l^2}} \quad (5)$$

183 and the GWMF at the surface is equal to

184 
$$\boldsymbol{\tau} = -\bar{\rho} \int_{-\infty}^{+\infty} \int_{-\infty}^{+\infty} \mathbf{v}' w' dx dy. \quad (6)$$

185 Here  $\bar{\rho}$  is the background air density, and  $\mathbf{v}' = (u', v')$  and  $w'$  are the perturbed horizontal and  
 186 vertical velocities in physical space, respectively. On substitution of the 2D Fourier transforms of  
 187  $\mathbf{v}'$  and  $w'$  into the above equation and using the polarization relation between  $\mathbf{v}'$  and  $w'$ , i.e.,  $\hat{\mathbf{v}} =$   
 188  $i \frac{\mathbf{K}}{K^2} \frac{\partial \hat{w}}{\partial z}$  (see the appendix of Xu et al. 2017b), one can readily obtain

189 
$$\boldsymbol{\tau} = 4\pi^2 \bar{\rho} \int_{-\infty}^{+\infty} \int_{-\infty}^{+\infty} \frac{\mathbf{K}}{K^2} \Im \left( \frac{\partial \hat{w}}{\partial z} \hat{w}^* \right) dk dl, \quad (7)$$

190 where  $\Im(\cdot)$  denotes the imaginary part of a complex number and the asterisk indicates complex  
 191 conjugate.

192 For the sake of computational convenience, elliptical polar coordinates are introduced, that  
 193 is,

194 
$$\tilde{k} = ak = \tilde{K} \cos \phi, \quad \tilde{l} = bl = \tilde{K} \sin \phi. \quad (8)$$

195 In this situation, the terrain spectrum has a simple form that only depends on  $\tilde{K}$ , i.e.,

196 
$$\hat{h}(\tilde{K}) = \frac{h_0 ab}{2\pi} e^{-\tilde{K}}. \quad (9)$$

197 Consequently, the GWMF can be expressed as

198 
$$\boldsymbol{\tau} = \frac{8\pi^2 \bar{\rho}}{b} \int_0^\pi \int_0^\infty (\cos \phi, \gamma \sin \phi) (\cos^2 \phi + \gamma^2 \sin^2 \phi)^{-1} \Im \left( \frac{\partial \hat{w}}{\partial z} \hat{w}^* \right) d\tilde{K} d\phi. \quad (10)$$

199 Substituting Eqs. (3) and (9) into the above equation yields

200 
$$\boldsymbol{\tau} = \Pi \int_0^\pi \int_0^{[Fr \cos(\phi - \chi)]^{-1}} (\cos \phi, \gamma \sin \phi) \frac{\cos(\phi - \chi)}{\sqrt{\cos^2 \phi + \gamma^2 \sin^2 \phi}} \sqrt{1 - [Fr \cos(\phi - \chi) \tilde{K}]^2} \tilde{K}^2 e^{-2\tilde{K}} d\tilde{K} d\phi, \quad (11)$$

202 where  $\Pi = 2\bar{\rho} N h_0^2 b |\tilde{\mathbf{V}}_0|$  and  $\chi = \text{atan} \left( \frac{\gamma V_0}{U_0} \right)$ . Note that  $\chi$  is the direction of  $\tilde{\mathbf{V}}_0 = (U_0, \gamma V_0)$ ,  
 203 which is similar to the actual wind  $\mathbf{V}_0$  but with the  $y$  velocity component scaled by the terrain  
 204 anisotropy. Only in the case of isotropic terrain (i.e.,  $\gamma = 1$ ) or when the horizontal wind is aligned

205 with the main axes of the orography (i.e.,  $U_0 = 0$  or  $V_0 = 0$ ) is  $\chi$  equal to the actual wind direction.  
 206 For simplicity, it is still called the horizontal wind direction hereafter, unless otherwise stated.

207 The non-dimensional parameter  $Fr$  is defined as  $Fr = \frac{|\tilde{V}_0|}{Na}$ , which represents a measure of  
 208 NHE. It is similar to the traditional Froude number ( $Fr = \frac{|V|}{Nh_0}$ ) that quantifies the nonlinearity of  
 209 OGWs (e.g., Miranda and James 1992), but with the mountain amplitude replaced by the mountain  
 210 width. It is thus called horizontal Froude number hereafter. Physically, the horizontal Froude  
 211 number can be viewed as the ratio between the period of buoyancy oscillation ( $1/N$ ) and the  
 212 advection time of airflow past the mountain ( $a/|\tilde{V}_0|$ ). In the limit  $Fr \rightarrow 0$ , i.e., slow airflow and/or  
 213 a broad mountain, the OGWs are predominantly hydrostatic. As  $Fr$  increases, NHE are more and  
 214 more important. In the limit  $Fr \rightarrow \infty$ , the airflow can quickly traverse the mountain, with no  
 215 internal OGWs excited.

216 In Eq. (11) the upper limit of the integral over  $\tilde{K}$  is  $[Fr \cos(\phi - \chi)]^{-1}$ , which indicates the  
 217 contribution to the GWMF coming from internal OGWs, because evanescent waves produce zero  
 218 GWMF. This upper limit depends on the directions of both the mean flow and the horizontal  
 219 wavenumber. To facilitate the deduction of the asymptotic GWMF expression (see section 3), this  
 220 upper limit is set to  $Fr^{-1}$ , i.e.,

$$221 \quad \tau_{\text{trunc}} = \Pi \int_0^\pi \int_0^{Fr^{-1}} (\cos\phi, \gamma \sin\phi) \frac{\cos(\phi - \chi)}{\sqrt{\cos^2\phi + \gamma^2 \sin^2\phi}} \sqrt{1 - [Fr \cos(\phi - \chi)\tilde{K}]^2} \tilde{K}^2 e^{-2\tilde{K}} d\tilde{K} d\phi. \quad (12)$$

223 This corresponds to an artificial truncation of waves with  $\tilde{K}$  between  $Fr^{-1}$  and  $[Fr \cos(\phi - \chi)]^{-1}$ .  
 224 The latter value can go up to infinity when  $\cos(\phi - \chi) \rightarrow 0$ . Nonetheless, as will be shown below,  
 225 these high-frequency waves only give a weak contribution to the total GWMF.

226

### 227 3 Asymptotic solution

228 Generally, a closed analytical form for Eq. (12) does not exist, and the GWMF must be  
 229 evaluated by numerical integration. Yet an asymptotic solution can be derived for weakly  
 230 nonhydrostatic OGWs at small  $Fr$  (see T08). In the limit  $Fr \rightarrow 0$ , the nonhydrostatic term in Eq.  
 231 (12) can be approximated by

$$232 \quad \sqrt{1 - [Fr \cos(\phi - \chi)\tilde{K}]^2} \approx 1 - \frac{1}{2}Fr^2 \cos^2(\phi - \chi)\tilde{K}^2, \quad (13)$$

233 based upon a Taylor series expansion around  $Fr = 0$  up to first order. On substitution of Eq. (13)  
 234 into (12), the asymptotic GWMF ( $\tau_{asy}$ ) is given by the sum of  $\tau_0$ ,  $\tau_{asy1}$ , and  $\tau_{asy2}$ , as follows

$$235 \quad \tau_0 = \Pi \int_0^\pi (\cos\phi, \gamma\sin\phi) \frac{\cos(\phi-\chi)}{\sqrt{\cos^2\phi+\gamma^2\sin^2\phi}} \left( \int_0^\infty \tilde{K}^2 e^{-2\tilde{K}} d\tilde{K} \right) d\phi, \quad (14a)$$

$$236 \quad \tau_{asy1} = -\Pi \int_0^\pi (\cos\phi, \gamma\sin\phi) \frac{\cos(\phi-\chi)}{\sqrt{\cos^2\phi+\gamma^2\sin^2\phi}} \left( \int_{Fr^{-1}}^\infty \tilde{K}^2 e^{-2\tilde{K}} d\tilde{K} \right) d\phi, \quad (14b)$$

$$237 \quad \tau_{asy2} = -\frac{1}{2}Fr^2 \Pi \int_0^\pi (\cos\phi, \gamma\sin\phi) \frac{\cos^3(\phi-\chi)}{\sqrt{\cos^2\phi+\gamma^2\sin^2\phi}} \left( \int_0^{Fr^{-1}} \tilde{K}^4 e^{-2\tilde{K}} d\tilde{K} \right) d\phi, \quad (14c)$$

238 with  $\tau_0 = (\tau_{0x}, \tau_{0y})$  denoting the GWMF of hydrostatic OGWs. In deriving these equations, we  
 239 have used  $\int_0^{Fr^{-1}} \tilde{K}^2 e^{-2\tilde{K}} d\tilde{K} = \int_0^\infty \tilde{K}^2 e^{-2\tilde{K}} d\tilde{K} - \int_{Fr^{-1}}^\infty \tilde{K}^2 e^{-2\tilde{K}} d\tilde{K}$ . Using integration by parts, it  
 240 is easy to show that

$$241 \quad \int_0^\infty \tilde{K}^2 e^{-2\tilde{K}} d\tilde{K} = \frac{1}{4}, \quad (15a)$$

$$242 \quad \int_{Fr^{-1}}^\infty \tilde{K}^2 e^{-2\tilde{K}} d\tilde{K} = \frac{1}{4}(2Fr^{-2} + 2Fr^{-1} + 1)e^{-2Fr^{-1}} = \frac{1}{4}I_2(Fr), \quad (15b)$$

$$243 \quad \int_0^{Fr^{-1}} \tilde{K}^4 e^{-2\tilde{K}} d\tilde{K} = \frac{1}{4}[3 - (2Fr^{-4} + 4Fr^{-3} + 6Fr^{-2} + 6Fr^{-1} + 3)e^{-2Fr^{-1}}] = \frac{1}{4}I_4(Fr). \quad (15c)$$

244 The  $I_2$  term receives contributions from wavenumbers ranging from  $\tilde{K} = Fr^{-1}$  to  $\tilde{K} = \infty$ . The  
 245 largest contribution of the integrand comes from  $\tilde{K} = 1$  (see the solid line in Fig. 1), which  
 246 corresponds to the typical horizontal scale of the orography. On the contrary, the  $I_4$  term is made

247 up of wavenumbers in the range between  $\tilde{K} = 0$  and  $\tilde{K} = Fr^{-1}$ , with the largest contribution from  
 248 the integrand being shifted to a higher wavenumber  $\tilde{K} = 2$  (i.e., half the orography scale; see the  
 249 dashed line in Fig. 1). The response decays rapidly away from  $\tilde{K} = 1$  for  $I_2$  and  $\tilde{K} = 2$  for  $I_4$ ,  
 250 especially towards the high-wavenumber tail of the spectrum (i.e., high-frequency waves). It is  
 251 noteworthy that this decay depends crucially on the exponential that results directly from the  
 252 Fourier transform of the terrain elevation, but any smooth topography will have a spectrum that  
 253 decays towards high wavenumbers (albeit in different ways). Substitution of Eq. (15) into (14)  
 254 yields

$$255 \quad \boldsymbol{\tau}_0 = \frac{\pi}{4} \int_0^\pi (\cos\phi, \gamma \sin\phi) \frac{\cos(\phi-\chi)}{\sqrt{\cos^2\phi + \gamma^2 \sin^2\phi}} d\phi, \quad (16a)$$

$$256 \quad \boldsymbol{\tau}_{asy1} = -I_2(Fr) \boldsymbol{\tau}_0, \quad (16b)$$

$$257 \quad \boldsymbol{\tau}_{asy2} = -\frac{1}{2} Fr^2 I_4(Fr) [R_x(\gamma, \chi) \tau_{0x}, R_y(\gamma, \chi) \tau_{0y}], \quad (16c)$$

258 where

$$259 \quad R_x(\gamma, \chi) = \frac{\int_0^\pi \frac{\cos\phi \cos^3(\phi-\chi)}{\sqrt{\cos^2\phi + \gamma^2 \sin^2\phi}} d\phi}{\int_0^\pi \frac{\cos\phi \cos(\phi-\chi)}{\sqrt{\cos^2\phi + \gamma^2 \sin^2\phi}} d\phi}, \quad (17a)$$

$$260 \quad R_y(\gamma, \chi) = \frac{\int_0^\pi \frac{\sin\phi \cos^3(\phi-\chi)}{\sqrt{\cos^2\phi + \gamma^2 \sin^2\phi}} d\phi}{\int_0^\pi \frac{\sin\phi \cos(\phi-\chi)}{\sqrt{\cos^2\phi + \gamma^2 \sin^2\phi}} d\phi}. \quad (17b)$$

261  $\boldsymbol{\tau}_{asy1}$  is anti-parallel to  $\boldsymbol{\tau}_0$ , with its magnitude controlled by the  $I_2$  term.  $\boldsymbol{\tau}_{asy2}$  is more complicated,  
 262 depending not only on  $Fr$  but also on  $\gamma$  and  $\chi$ . Given the difference between  $R_x$  and  $R_y$ ,  $\boldsymbol{\tau}_{asy2}$  may  
 263 be misaligned with  $\boldsymbol{\tau}_0$ . This suggests that NHE can change the direction of the GWMF as well as  
 264 its magnitude.

265 In order to better understand the NHE, they are quantified by the ratio between the  
 266 asymptotic and hydrostatic GWMFs, i.e.,

$$267 \quad \tilde{\tau}_x(Fr, \gamma, \chi) = \frac{\tau_{asyx}}{\tau_{x0}} = 1 - I_2(Fr) - \frac{1}{2}Fr^2 I_4(Fr) R_x(\gamma, \chi), \quad (18a)$$

$$268 \quad \tilde{\tau}_y(Fr, \gamma, \chi) = \frac{\tau_{asyy}}{\tau_{y0}} = 1 - I_2(Fr) - \frac{1}{2}Fr^2 I_4(Fr) R_y(\gamma, \chi). \quad (18b)$$

269 The second term on the right-hand-side (RHS) of Eq. (18) is related to  $\mathbf{\tau}_{asy1}$  (hereafter, NHE1 for  
 270 short), which only depends on the horizontal Froude number. It denotes the wave components that  
 271 are mistaken as vertically-propagating internal waves in the hydrostatic approximation, but are  
 272 actually evanescent waves. The third term arises from  $\mathbf{\tau}_{asy2}$  (hereafter, NHE2 for short), which is  
 273 attributed to the difference between the dispersion relationships of hydrostatic and nonhydrostatic  
 274 OGWs, i.e., the  $K^2$  term within the brackets of Eq. (1). As noted above, NHE2 can affect both the  
 275 magnitude and direction of the GWMF.

276 The above asymptotic expressions were derived for weakly nonhydrostatic OGWs. In the  
 277 limit  $Fr \rightarrow 0$ , they simplify to

$$278 \quad \tilde{\tau}_x(Fr \rightarrow 0, \gamma, \chi) = 1 - \frac{3}{2}R_x(\gamma, \chi)Fr^2, \quad (19a)$$

$$279 \quad \tilde{\tau}_y(Fr \rightarrow 0, \gamma, \chi) = 1 - \frac{3}{2}R_y(\gamma, \chi)Fr^2. \quad (19b)$$

280 As will be shown in section 4, the relative difference between the asymptotic and exact GWMFs  
 281 increases as the horizontal Froude number increases. Therefore, the asymptotic GWMF at  $Fr \rightarrow$   
 282  $\infty$  provides an estimate of the upper bound of the bias. Expanding the  $e^{-2Fr^{-1}}$  term in Eq. (18) as  
 283  $Fr \rightarrow \infty$  using Taylor series, one can readily find that

$$284 \quad \tilde{\tau}_x(Fr \rightarrow \infty, \gamma, \chi) = \left[ \frac{4}{3} - \frac{2}{5}R_x(\gamma, \chi) \right] Fr^{-3}, \quad (20a)$$

$$285 \quad \tilde{\tau}_y(Fr \rightarrow \infty, \gamma, \chi) = \left[ \frac{4}{3} - \frac{2}{5}R_y(\gamma, \chi) \right] Fr^{-3}. \quad (20b)$$

286 At this highly-nonhydrostatic limit, the GWMF becomes extremely small (proportional to  $Fr^{-3}$ ),  
 287 given the trivial contribution from very small-scale OGWs (see Fig. 1). This result is not only  
 288 qualitatively correct, given that, without adopting the approximation expressed by Eq. (13), the  
 289 drag would also decrease to zero at high  $Fr$ , but even approximately quantitatively correct, as will  
 290 be shown next.

291

## 292 **4 Results**

293 In this section, the NHE will be firstly studied for the simple case of a circular mountain,  
 294 i.e.,  $\gamma = 1$ . Then we will investigate the more general case of elliptical mountains with  $\gamma \neq 1$ . In  
 295 the latter case, the mean flow can be either parallel or oblique to the main axes of the mountain,  
 296 which will be examined separately. These variants will henceforth be called “parallel flow” and  
 297 “oblique flow”, for short.

### 298 4.1 Isotropic terrain

299 For isotropic terrain, without loss of generality, the horizontal wind direction can be set to  
 300  $\chi = 0$  for simplicity, i.e.,  $\mathbf{V}_0 = (U_0, 0)$ . In this case,  $\tau_{x0} = \frac{\pi}{4} \bar{\rho} N h_0^2 a U_0$ ,  $\tau_{y0} = 0$ ,  $R_x(1, 0) = \frac{3}{4}$ ,  
 301  $R_y(1, 0) = 0$ , and Eq. (18) simplifies to

$$\begin{aligned}
 302 \quad \tilde{\tau}_c(Fr) &= 1 - I_2(Fr) - \frac{3}{8} Fr^2 I_4(Fr) \\
 303 \quad &= 1 - \frac{9}{8} Fr^2 + e^{-2Fr^{-1}} \left( -\frac{5}{4} Fr^{-2} - \frac{1}{2} Fr^{-1} + \frac{5}{4} + \frac{9}{4} Fr + \frac{9}{8} Fr^2 \right), \quad (21)
 \end{aligned}$$

304 where the subscript “c” indicates circular terrain. Clearly,  $\tilde{\tau}_c$  only depends on the horizontal Froude  
 305 number.

306 The variation of  $\tilde{\tau}_c$  with the horizontal Froude number is depicted in Fig. 2. For comparison,  
 307 the scaled asymptotic GWMF in the case of 2D ridge is also shown, which is expressed as follows  
 308 [cf. Eq. (16) in T08]

309 
$$\tilde{\tau}_{2D}(Fr) = \frac{\tau_{asy-2D}}{\tau_{0-2D}} = 1 - \frac{3}{4}Fr^2 + e^{-2Fr^{-1}} \left( -Fr^{-1} + \frac{1}{2} + \frac{3}{2}Fr + \frac{3}{4}Fr^2 \right). \quad (22)$$

310 It is clear that NHE weaken the GWMF. For both 2D and 3D OGWs, the asymptotic GWMFs are  
 311 in good agreement with their exact counterparts which are obtained via numerical integration of  
 312 Eq. (11) in this work and Eq. (10) in T08, respectively. The GWMF is only slightly overestimated  
 313 by Eq. (22) for 2D flow and underestimated by Eq. (12) with respect to Eq. (11) for 3D flow for  
 314 moderate  $Fr$ . This justifies the choice of  $Fr^{-1}$  as the upper limit of the integral in Eq. (11), given  
 315 the simplifications this entails. Although adoption of the asymptotic approximation for the GWMF  
 316 slightly improves the agreement with Eq. (11), the GWMF is still underestimated by a larger  
 317 fraction than it is overestimated in the 2D case. Note that  $\tilde{\tau}_c$  is always smaller than its 2D  
 318 counterpart. In the limit  $Fr \rightarrow 0$ ,  $\tilde{\tau}_c(Fr)$  tends asymptotically to  $1 - \frac{9}{8}Fr^2$  while  $\tilde{\tau}_{2D}$  varies as  
 319  $1 - \frac{3}{4}Fr^2$ . In the opposite limit  $Fr \rightarrow \infty$ ,  $\tilde{\tau}_c$  and  $\tilde{\tau}_{2D}$  tend asymptotically to

320 
$$\tilde{\tau}_c(Fr \rightarrow \infty) = \frac{31}{30}Fr^{-3}, \quad (23)$$

321 
$$\tilde{\tau}_{2D}(Fr \rightarrow \infty) = \frac{3}{2}Fr^{-2}, \quad (24)$$

322 respectively.  $\tilde{\tau}_c$  is proportional to  $Fr^{-3}$  which decays faster than  $\tilde{\tau}_{2D}$ . As shown by Fig. 2, the way  
 323 in which  $\tilde{\tau}_c$  approaches zero as  $Fr$  increases is surprisingly accurate (as found in T08 for  $\tilde{\tau}_{2D}$ )  
 324 given that the asymptotic approximation was developed for small  $Fr$ .

325 As stated in section 3, the NHE can be decomposed into two terms: NHE1 and NHE2.  
 326 Figure 3 displays these two terms as a function of the horizontal Froude number. The magnitude  
 327 of NHE1 exhibits an increasing trend with  $Fr$ . At lower horizontal Froude numbers ( $Fr < 0.2$ ), the  
 328 NHE1 term is very weak. This is because the lower limit of the integral in Eq. (15b) is given by  
 329  $Fr^{-1}$ , hence the NHE1 term mainly comes from high-frequency waves which produce negligible  
 330 GWMF (Fig. 1). As  $Fr$  increases beyond 0.2 (corresponding to a cutoff horizontal wavenumber of

331  $\tilde{K} = 5$ ), the magnitude of NHE1 term increases rapidly, reaching up to about 0.7 at  $Fr = 1$ . As  $Fr$   
332 approaches infinity, this term tends asymptotically to -1. The NHE2 term is jointly determined by  
333 the squared horizontal Froude number ( $Fr^2$ ) and  $I_4$  given by Eq. (15c). As the horizontal Froude  
334 number increases, each of these two factors increases and decreases, respectively. The latter effect  
335 is due to the fact that the upper limit of the integral in Eq. (15c) decreases as  $Fr$  increases. As a  
336 result, the magnitude of NHE2 firstly increases with  $Fr$ , peaking around  $Fr = 0.48$  at a maximum  
337 of about 0.1. It then starts decreasing as the horizontal Froude number increases. It is clear that  
338 NHE2 plays a more important role in the flow regimes with low  $Fr$  whereas NHE1 dominates  
339 above about  $Fr = 0.4$ .

#### 340 4.2 Anisotropic terrain: parallel flow

341 For OGWs generated by elliptical mountains, we firstly study the special case of horizontal  
342 wind parallel to the main axes of the orography, which are assumed to be aligned in the  $x$  and  $y$   
343 directions, i.e.,  $\chi = 0$  (mean flow along the  $x$  axis) or  $\chi = \pm \frac{\pi}{2}$  (mean flow along the  $y$  axis). In  
344 this situation,  $\tilde{\tau}$  only depends on the horizontal Froude number and on the terrain anisotropy.

345 Taking  $\chi = 0$  for example, i.e.,  $\mathbf{V}_0 = (U_0, 0)$ , one obtains that  $\tau_{y0} = 0$ ,  $R_y(\gamma, 0) = 0$ , and

$$346 \quad R_{x0}(\gamma) = R_x(\gamma, 0) = \frac{\int_0^\pi \frac{\cos^4 \phi}{\sqrt{\cos^2 \phi + \gamma^2 \sin^2 \phi}} d\phi}{\int_0^\pi \frac{\cos^2 \phi}{\sqrt{\cos^2 \phi + \gamma^2 \sin^2 \phi}} d\phi}. \quad (25)$$

347 Hereafter, the subscript “0” denotes the case with  $\chi = 0$ . The black line in Fig. 4 shows the  
348 variation of  $R_{x0}(\gamma)$  with  $\gamma$ . Clearly,  $R_{x0}(\gamma)$  increases as  $\gamma$  increases (i.e., from a ridge normal to  
349 the flow to a ridge along the flow direction), showing substantial changes (by about 30%) from  
350  $\gamma = \frac{1}{10}$  to  $\gamma = 10$ . The fastest variation occurs near  $\gamma = 1$ .

351 To better reveal the influence of terrain anisotropy, the relative variation of  $\tilde{\tau}_{x0}(\gamma, Fr)$  with  
 352 respect to  $\tilde{\tau}_c$  is examined, which is defined as

$$353 \quad \Delta\tilde{\tau}_{x0}(\gamma, Fr) = \frac{\tilde{\tau}_{x0}(\gamma, Fr) - \tilde{\tau}_c(Fr)}{\tilde{\tau}_c(Fr)} = \frac{\tilde{\tau}_{x0}(\gamma, Fr)}{\tilde{\tau}_c(Fr)} - 1. \quad (26)$$

354 At  $Fr = 0$ ,  $\Delta\tilde{\tau}_{x0}$  is always equal to zero (Fig. 5). As the horizontal Froude number increases, the  
 355  $\Delta\tilde{\tau}_{x0}$  curves quickly diverge. In the case of mean flow perpendicular to the long axis of the  
 356 mountain ( $\gamma < 1$ ),  $\Delta\tilde{\tau}_{x0}$  is greater than zero, i.e.,  $\tilde{\tau}_{x0}(\gamma, Fr) > \tilde{\tau}_c(Fr)$ . This means that the  
 357 GWMF is less reduced than in the isotropic case, i.e., weakening of NHE. This is consistent with  
 358 the 2D-3D comparison presented in Fig. 2. In contrast, when the mean flow is aligned with the  
 359 long axis of the mountain ( $\gamma > 1$ ), NHE are enhanced, as suggested by the negative  $\Delta\tilde{\tau}_{x0}$ .

360 The  $\Delta\tilde{\tau}_{x0}$  curves become more and more flat as the horizontal Froude number increases,  
 361 tending asymptotically to their limits at  $Fr \rightarrow \infty$ , i.e.,

$$362 \quad \Delta\tilde{\tau}_{x0}(\gamma, Fr \rightarrow \infty) = \frac{9}{31} \left[ 1 - \frac{4}{3} R_{x0}(\gamma) \right], \quad (27)$$

363 which is obtained on substitution of Eqs. (20a) and (23) into Eq. (26). It is clear that the influence  
 364 of terrain anisotropy is controlled by  $R_{x0}(\gamma)$ . When the mean flow is aligned with the long axis of  
 365 the mountain, (the magnitude of)  $\Delta\tilde{\tau}_{x0}$  is more notably enhanced than it is suppressed in the case  
 366 of mean flow perpendicular to the long axis of the mountain. For instance, at  $Fr = 1$ ,  $\Delta\tilde{\tau}_{x0}$  exceeds  
 367 3% at  $\gamma = 8$  while it is less than 3% at  $\gamma = \frac{1}{8}$ . This difference is attributed to the asymmetric  
 368 distribution of  $R_{x0}(\gamma)$  about  $\gamma = 1$  (see the black line in Fig. 4).

369 While  $R_{x0}(\gamma)$  changes substantially with  $\gamma$ , that is not so much the case of  $\Delta\tilde{\tau}_{x0}$ . For two  
 370 arbitrary  $\gamma$ , say,  $(\gamma_1, \gamma_2)$ , the difference between their  $\Delta\tilde{\tau}_{x0}$  gradually saturates as  $Fr \rightarrow \infty$ , i.e.,

$$371 \quad \Delta\tilde{\tau}_{x0}(\gamma_1, Fr \rightarrow \infty) - \Delta\tilde{\tau}_{x0}(\gamma_2, Fr \rightarrow \infty) = \frac{12}{31} [R_{x0}(\gamma_2) - R_{x0}(\gamma_1)]. \quad (28)$$

372 This means that the influence of terrain anisotropy on  $R_{x0}(\gamma)$  can be only partially projected onto  
373  $\Delta\tilde{\tau}_{x0}$ , since the latter is at most  $\frac{12}{31} \approx 40\%$  of the former. From Eq. (25),  $R_{x0}(\gamma)$  equals  $\frac{2}{3}$  and 1 at  
374  $\gamma = 0$  and  $\gamma \rightarrow \infty$ , respectively. Bounded by the lower and upper limits of  $R_{x0}(\gamma)$ , the variation  
375 of  $\Delta\tilde{\tau}_{x0}$  with  $\gamma$  is thus always smaller than  $\frac{12}{31} \times \left(1 - \frac{2}{3}\right) = \frac{4}{31} \approx 12.9\%$ . When compared to NHE  
376 in the isotropic orography case, i.e.,  $R_{x0}(1) = \frac{3}{4}$ , the maximum positive and negative differences  
377 are  $\frac{12}{31} \times \left(1 - \frac{3}{4}\right) = \frac{3}{31} \approx 9.7\%$  and  $\frac{12}{31} \times \left(\frac{2}{3} - \frac{3}{4}\right) = -\frac{1}{31} \approx -3.2\%$ , respectively.

378 From the above analysis, we can see that NHE in the parallel-flow case are only weakly  
379 affected by terrain anisotropy. Instead, it is the horizontal Froude number that greatly impacts  $\tilde{\tau}_{x0}$ ,  
380 and this occurs both in the cases of circular mountains and 2D ridges (see section 4.1). Physically,  
381 when the mean flow is parallel to the main axis of the elliptical terrain, e.g., when  $\chi = 0$ , as studied,  
382 the horizontal Froude number is simplified to  $Fr = \frac{|\tilde{V}_0|}{Na} = \frac{U_0}{Na}$ . Thus, the terrain width in the cross-  
383 flow direction has little contribution to the flow advection time.

### 384 4.3 Anisotropic terrain: oblique flow

385 In this section, the general case of mean flow oblique to the main axes of the elliptical bell-  
386 shaped mountain is examined to understand more thoroughly the impacts of terrain anisotropy and  
387 horizontal wind direction on the asymptotic GWMF expression.

388 In addition to  $\chi = 0$ , Figure 4 also shows the variation of  $R_x(\gamma, \chi)$  as a function of  $\gamma$  for  
389 three different horizontal wind directions, i.e.,  $\chi = \frac{\pi}{8}, \frac{\pi}{4}$  and  $\frac{3\pi}{8}$ . These wind directions are chosen  
390 in the range of  $\left[0, \frac{\pi}{2}\right)$ , but the same results can be obtained for  $\chi$  in the range of  $\left[0, -\frac{\pi}{2}\right)$ . This is  
391 because  $R_x(\gamma, \chi)$  is symmetric about  $\chi = 0$ , i.e.,  $R_x(\gamma, \chi) = R_x(\gamma, -\chi)$  in accordance with Eq.  
392 (17a). (Note that  $R_x(\gamma, \chi)$  is ill-defined at  $\chi = \pm\frac{\pi}{2}$  where  $\tau_{x0}$  vanishes.) The variation of  $R_y(\gamma, \chi)$

393 is not presented herein, but can be inferred from that of  $R_x(\gamma, \chi)$  because  $R_x(\gamma, \chi) =$   
394  $R_y\left(\frac{1}{\gamma}, \frac{\pi}{2} - \chi\right)$ . In the situation with  $\chi = \frac{\pi}{8}$ ,  $R_x(\gamma, \chi)$  increases as  $\gamma$  increases, which is similar to  
395 the case with  $\chi = 0$ . When  $\chi$  equals  $\frac{\pi}{4}$  or  $\frac{3\pi}{8}$ ,  $R_x(\gamma, \chi)$  instead decreases as  $\gamma$  increases. This  
396 suggests a change in the trend of  $R_x(\gamma, \chi)$  with  $\gamma$  for a horizontal wind direction between  $\chi = \frac{\pi}{8}$   
397 and  $\chi = \frac{\pi}{4}$ , at which  $R_x(\gamma, \chi)$  should be independent of  $\gamma$ . As can be seen below, this occurs at  
398  $\chi = \frac{\pi}{6}$ .

399 The distribution of  $R_x(\gamma, \chi)$  in  $\gamma$ - $\chi$  parameter space is shown in Fig. 6, with  $\gamma$  and  $\chi$  in the  
400 ranges of  $\left[\frac{1}{10}, 10\right]$  and  $\left[0, \frac{\pi}{2}\right)$ , respectively.  $R_x(\gamma, \chi)$  is always equal to  $\frac{3}{4}$  at  $\chi = \frac{\pi}{6}$ , which can be  
401 obtained analytically from Eq. (17a). Remember that  $R_x(\gamma, \chi) \equiv \frac{3}{4}$  at  $\gamma = 1$  as well (see section  
402 4.1). Therefore, the  $\gamma$ - $\chi$  space can be divided into four quadrants by the lines  $\chi = \frac{\pi}{6}$  and  $\gamma = 1$ . In  
403 the third and fourth quadrants ( $0 \leq \chi < \frac{\pi}{6}$ ),  $R_x(\gamma, \chi)$  has an increasing trend with  $\gamma$ . The more the  
404 horizontal wind is aligned with the long axis of the elliptical mountain, the more markedly terrain  
405 anisotropy affects  $R_x(\gamma, \chi)$ . The greatest variation of  $R_x(\gamma, \chi)$  with  $\gamma$  ( $R_{x0}(\gamma \rightarrow \infty) - R_{x0}(\gamma \rightarrow$   
406  $0)$ ) occurs at  $\chi = 0$ , which takes the value  $\frac{1}{3}$ , as derived in section 4.2. In the first and second  
407 quadrants (i.e.,  $\frac{\pi}{6} < \chi < \frac{\pi}{2}$ ),  $R_x(\gamma, \chi)$  decreases instead as  $\gamma$  increases, and the influence of terrain  
408 anisotropy becomes larger with  $\chi$ . In the limit of  $\chi = \frac{\pi}{2}$ ,  $R_x\left(\gamma, \frac{\pi}{2}\right)$  is ill-defined, yet it is equivalent  
409 to  $R_y\left(\frac{1}{\gamma}, 0\right)$  which is well defined. From Eq. (17b),  $R_x\left(\gamma \rightarrow 0, \frac{\pi}{2}\right) = R_y(\gamma \rightarrow \infty, 0) = 1$ , and  
410  $R_x\left(\gamma \rightarrow \infty, \frac{\pi}{2}\right) = R_y(\gamma \rightarrow 0, 0) = \frac{1}{3}$ . As a result, the greatest variation of  $R_x(\gamma, \chi)$  with  $\gamma$  is  $\frac{2}{3}$ , i.e.  
411 twice that for  $\chi = 0$ . Similarly, the greatest variations of  $R_x(\gamma, \chi)$  with  $\chi$  (i.e., variations along the

412 vertical rather than horizontal direction in the graph) on the left- and right semi-planes of the  $\gamma$ - $\chi$   
 413 parameter space are  $\frac{1}{3}$  and  $\frac{2}{3}$ , respectively.

414 As in the parallel-flow case, the relative variation of  $\tilde{\tau}_x(\gamma, Fr)$  with respect to  $\tilde{\tau}_c$  is also  
 415 examined here, which is defined as

$$416 \quad \Delta\tilde{\tau}_x(\gamma, \chi, Fr) = \frac{\tilde{\tau}_x(\gamma, \chi, Fr) - \tilde{\tau}_c(Fr)}{\tilde{\tau}_c(Fr)} = \frac{\tilde{\tau}_x(\gamma, \chi, Fr)}{\tilde{\tau}_c(Fr)} - 1. \quad (29)$$

417 As  $Fr \rightarrow \infty$ ,  $\tilde{\tau}_x$  tends asymptotically to

$$418 \quad \tilde{\tau}_x(\gamma, \chi, Fr \rightarrow \infty) = \frac{9}{31} \left[ 1 - \frac{4}{3} R_x(\gamma, \chi) \right]. \quad (30)$$

419 For two pairs of  $(\gamma, \chi)$ , e.g.,  $(\gamma_1, \chi_1)$  and  $(\gamma_2, \chi_2)$ , the difference between their  $\tilde{\tau}_x$  is

$$420 \quad \tilde{\tau}_x(\gamma_1, \chi_1, Fr \rightarrow \infty) - \tilde{\tau}_x(\gamma_2, \chi_2, Fr \rightarrow \infty) = \frac{12}{31} [R_x(\gamma_2, \chi_2) - R_x(\gamma_1, \chi_1)]. \quad (31)$$

421 Again, this means that the influences of terrain anisotropy and horizontal wind direction on  
 422  $R_x(\gamma, \chi)$  have a relatively small impact on  $\tilde{\tau}_x$ . From Fig. 6, the global maximal variation of  
 423  $R_x(\gamma, \chi)$  with  $\gamma$  and  $\chi$  is  $\frac{2}{3}$ . Thus, under the influence of both terrain anisotropy and horizontal

424 wind direction,  $\tilde{\tau}_x$  can change by  $\frac{12}{31} \times \frac{2}{3} \approx 25.8\%$  at most as  $Fr$  tends to infinity. Compared to the

425 NHE in the isotropic terrain case, the maximum positive and negative differences are

$$426 \quad \frac{12}{31} \times \left( 1 - \frac{3}{4} \right) = \frac{3}{31} \approx 9.7\% \text{ and } \frac{12}{31} \times \left( \frac{1}{3} - \frac{3}{4} \right) = -\frac{5}{31} \approx -16.1\%, \text{ respectively. At small horizontal}$$

427 Froude number, the impacts of terrain anisotropy and horizontal wind direction are rather weak,

428 as will be shown below.

429 Figure 7 gives the distributions of  $\Delta\tilde{\tau}_x$  on the  $\gamma$ - $\chi$  plane at four different horizontal Froude

430 numbers:  $Fr = 0.1, 0.3, 0.5,$  and  $1.0$ , respectively. Positive  $\Delta\tilde{\tau}_x$  is found in the first and third

431 quadrants, indicating an amplification of the NHE compared to the case of isotropic orography.

432 Conversely, NHE are weakened in the second and fourth quadrants, given the negative values of

433  $\Delta\tilde{\tau}_x$  existing there. At  $Fr = 0.1$  (Fig. 7a)  $\Delta\tilde{\tau}_x$  is extremely small, implying that the terrain  
 434 anisotropy and horizontal wind direction have negligible influence on the NHE. At  $Fr = 0.3$  (Fig.  
 435 7b), the impacts of terrain anisotropy and horizontal wind direction increase by more than 10 times  
 436 compared to those at  $Fr = 0.1$ . When the horizontal Froude number further increases to  $Fr = 0.5$   
 437 and 1.0 (Figs. 7c, 7d), there occurs a consistent increase in the magnitude of  $\Delta\tilde{\tau}_x$ , which can reach  
 438 up to 0.1 in the first quadrant (i.e.,  $\gamma > 1$  and  $\frac{\pi}{6} < \chi < \frac{\pi}{2}$ ).

439 Figure 8 displays the variation of  $\tilde{\tau}_x$  as a function of  $Fr$ . Two elliptical mountains with  $\gamma =$   
 440  $\frac{1}{8}$  (dashed lines) and  $\gamma = 8$  (solid lines) are selected, along with two horizontal wind directions  
 441  $\chi = \frac{\pi}{8}$  (blue lines) and  $\chi = \frac{3\pi}{8}$  (red lines). From the above analysis, these configurations of terrain  
 442 anisotropy and horizontal wind direction tend to have a significant influence on the NHE. However,  
 443 as can be seen from Fig. 8,  $\tilde{\tau}_x$  is still mainly determined by  $Fr$ . At  $Fr = 0.1$ ,  $\tilde{\tau}_x = 0.99$ , i.e., the  
 444 OGWs are almost purely hydrostatic. As  $Fr$  increases,  $\tilde{\tau}_x$  decreases rapidly to about 0.65 at  $Fr =$   
 445 0.5, and further reduces to about 0.27 at  $Fr = 1.0$ . Compared with the horizontal Froude number,  
 446 terrain anisotropy and horizontal wind direction only play a minor role. This is due to the fact that  
 447 these two factors only affect the NHE2 term [see Eq. (18)]. At small horizontal Froude number  
 448 ( $Fr < 0.2$ ), the NHE2 term is of greater importance than NHE1 (Fig. 2), but  $\Delta\tilde{\tau}_x$  is too weak to  
 449 exert a profound influence on  $\tilde{\tau}_x$  (Fig. 7a). At moderate to large horizontal Froude number ( $Fr >$   
 450 0.4), while  $\Delta\tilde{\tau}_x$  is significantly enhanced (Figs. 7c, 7d), the NHE2 term is exceeded by NHE1, thus  
 451 contributing less to  $\tilde{\tau}_x$ .

#### 452 4.4 Surface pressure perturbation

453 Theoretically, the GWMF is equal to the pressure drag at the surface (e.g., Teixeira et al.  
 454 2004). In this section, the surface pressure perturbations are investigated to help understand the  
 455 impact of NHE on the GWMF. Herein, we only focus on the simple case of mean flow over circular

456 bell-shaped mountains, because the horizontal wind direction and orography anisotropy play a  
457 minor role on the NHE (as we have just seen).

458 Figure 9 depicts the distribution of the surface pressure perturbation obtained via numerical  
459 integration of Eqs. (A4). Note that the pressure perturbations are scaled with  $\bar{\rho}N|\tilde{\mathbf{V}}|h_0$ . At  $Fr =$   
460 0.1, the pressure field (Fig. 9a) shows a left-right anti-symmetric pattern about the orography  
461 center, with positive and negative regions on the windward and leeward slope respectively (Smith  
462 1980; Teixeira et al. 2004). In this weakly nonhydrostatic case, the pressure perturbation mainly  
463 arises from vertically-propagating OGWs, with little contribution from evanescent waves (Figs.  
464 9b, 9c). At  $Fr = 0.5$ , however, the surface pressure perturbation ceases to be perfectly anti-  
465 symmetric about the mountain center (Fig. 9d). The maximum on the windward slope weakens  
466 slightly as compared to that at  $Fr = 0.1$ , while the minimum on the lee slope also weakens notably  
467 and moves downstream. In addition, a secondary pressure minimum occurs near the orography  
468 center. This more complex pressure pattern is due to an enhanced pressure contribution from  
469 evanescent waves (Fig. 9f), which is symmetric about the orography center (and thus produces  
470 zero surface pressure drag). Concurrently, the pressure perturbation associated with vertically-  
471 propagating OGWs weakens (Fig. 9e), giving rise to the reduction of GWMF.

472 Using the Taylor series expansion of the vertical wavenumber at small  $Fr$  (expressed by  
473 Eq. (13)), one can also derive an asymptotic expression for the pressure perturbation associated  
474 with vertically-propagating OGWs (see details in Appendix A), which is decomposed into three  
475 parts (namely,  $p_0$ ,  $p_1$  and  $p_2$ ) corresponding to  $\boldsymbol{\tau}_0$ ,  $\boldsymbol{\tau}_{asy1}$  and  $\boldsymbol{\tau}_{asy2}$ , respectively.

476 Figure 10 shows the distribution of the asymptotic surface pressure perturbation at  $Fr =$   
477 0.1, which is also scaled by  $\bar{\rho}N|\tilde{\mathbf{V}}|h_0$ . The total asymptotic pressure perturbation (Fig. 10a) agrees  
478 well with that in Fig. 9a. It is dominated by the hydrostatic part (Fig. 10b), because NHE are very

479 weak at  $Fr = 0.1$  (see Fig. 2). The maximum (minimum) pressure perturbation occurs about one  
 480 half-width away from the orography center, suggesting that the horizontal scale of the dominant  
 481 wave field is comparable to that of the mountain. This is consistent with the power spectrum of  $\tau_0$ ,  
 482 which peaks at  $\tilde{K} = 1$ , i.e.,  $K = a^{-1}$  (Fig. 1). The  $p_1$  pressure perturbation is extremely small (Fig.  
 483 10c), given the small magnitude of  $\tau_{asy1}$  at this low horizontal Froude number (Fig. 3). A wave-  
 484 train pattern is found both upstream and downstream of the mountain, which can be ascribed to  
 485 the  $\cos\left(\frac{\mu}{Fr}\right)$  and  $\sin\left(\frac{\mu}{Fr}\right)$  terms in Eq. (A9b). This pattern is indiscernible in Fig. 10a because of  
 486 its small magnitude. The horizontal wavelength of  $p_1$  is very short, since it originates mainly from  
 487 the high-frequency part of the wave spectrum [Eq. (A7b)]. Similar to  $p_0$ , the  $p_2$  pressure  
 488 perturbation is anti-symmetric about the orography center (Fig. 10d), but with negative (positive)  
 489 perturbations on the upslope (downslope) side. Consequently,  $p_2$  produces a pressure gradient  
 490 force opposed to that of  $p_0$ , contributing negatively to the total surface pressure drag. Moreover,  
 491 the  $p_2$  pressure perturbation is mainly confined to the region within one half-width of the mountain  
 492 to the orography center. This is also in agreement with the power spectrum of  $\tau_{asy2}$  which peaks  
 493 at  $\tilde{K} = 2$  (Fig. 1).

494 Figure 11 is similar to Fig. 10, but for  $Fr = 0.5$ . Compared to that at  $Fr = 0.1$ , the total  
 495 pressure perturbation is substantially reduced (Fig. 11a). The pressure perturbation extrema only  
 496 correspond to about 70% of those at  $Fr = 0.1$ . The scaled  $p_0$  (Fig. 11b) is independent of  $Fr$ , so it  
 497 is exactly the same as in Fig. 10b. The  $p_1$  pressure perturbation (Fig. 11c) increases markedly in  
 498 magnitude, reaching up to 60% of  $p_0$ . The  $p_2$  pressure perturbation is also enhanced (Fig. 11d).  
 499 However, unlike in the case with  $Fr = 0.1$ ,  $p_2$  is smaller than  $p_1$ . This agrees with the major role  
 500 played by the NHE1 term at moderate-to-large horizontal Froude numbers (see Fig. 3). Moreover,  
 501 while the  $p_1$  and  $p_2$  pressure perturbations still display a wave-train pattern upstream and

502 downstream of the mountain, their horizontal wavelengths have increased significantly. Taking  $p_1$   
503 as an example, the dominant wavelength is approximately twice the orography half-width. This is  
504 because, at  $Fr = 0.5$ ,  $p_1$  is composed of wavenumbers ranging from  $\tilde{K} = 2$  to  $\infty$  [see Eq. (A7b)].  
505 In this spectral range, the greatest response of  $\tau_{asy1}$  corresponding to  $p_1$  occurs at  $\tilde{K} = 2$  (Fig. 1).  
506 Owing to the enhanced  $p_1$  pressure perturbation, the extrema of the total pressure perturbation  
507 slightly move away from the orography center (Fig. 11a), implying an increase in the dominant  
508 wavelength. This is reasonable, since short waves are removed by the NHE from the range of  
509 waves that contribute to the GWMF.

510

## 511 **5 Summary and discussion**

512 It has been widely recognized that the parameterization of subgrid-scale orographic gravity  
513 waves (OGWs) is essential for accurate numerical weather forecast and climate prediction. Many  
514 efforts have been made to improve the representation of orographic gravity wave momentum flux  
515 (GWMF) and its deposition into the mean flow in numerical models. With the development of  
516 high-resolution global numerical weather prediction (NWP) and general circulation models  
517 (GCMs), the horizontal scale of unresolved OGWs is becoming increasingly small. As a result,  
518 the GWMF can be significantly impacted by nonhydrostatic effects (NHE). However, these effects  
519 are not accounted for in even the state-of-the-art parameterization schemes, since there is in general  
520 no analytical solution for nonhydrostatic OGWs. In some parametrizations (e.g., Lott and Miller  
521 1997), the GWMF reduction that is known to occur for highly non-hydrostatic waves is mimicked  
522 rather artificially by filtering the orography that is fed into the OGW parametrization. The present  
523 study proposes the more physical approach of explicitly evaluating the NHE approximately.

524 Using linear gravity wave theory, we have derived an asymptotic solution for the surface  
525 GWMF of 3D OGWs, which is an extension of the 2D asymptotic expression studied in T08. The  
526 intensity of the NHE can be quantified by the non-dimensional parameter called here the horizontal  
527 Froude number, i.e.,  $Fr = \frac{|\tilde{V}_0|}{Na}$ . This parameter is akin to the inverse non-dimensional mountain  
528 half width  $\frac{Na}{U}$  used in previous studies (e.g., Durran and Klemp 1983; Xue and Thorpe 1991; Zängl  
529 2003) but with  $U$  replaced by  $\tilde{V}_0 = (U_0, \gamma V_0)$ . This extended definition is necessary due to the  
530 horizontal anisotropy of the isolated orography that generates the 3D OGWs.

531 Based upon an asymptotic approach, the NHE are divided into two components (NHE1  
532 and NHE2). The first component accounts for the high-frequency parts of the wave spectrum (i.e.,  
533 short waves) that are mistaken as hydrostatic, upward-propagating waves in the hydrostatic  
534 approximation. The GWMF associated with NHE1 is parallel but opposite to the hydrostatic  
535 GWMF. The second component is due to the difference between the dispersion relationships of  
536 hydrostatic and nonhydrostatic OGWs. While NHE1 only depends on the horizontal Froude  
537 number, NHE2 also depends on the terrain anisotropy and horizontal wind direction. In the  
538 presence of NHE, both the magnitude and direction of GWMF can be changed.

539 The asymptotic GWMF expression derived here was investigated for OGWs forced by both  
540 circular and elliptical mountains for flows with various orientations. In the isotropic orography  
541 case, NHE only depend on the horizontal Froude number, which is the same dependence as in the  
542 2D-ridge case studied by T08. Compared to its 2D counterpart, the 3D GWMF is more strongly  
543 reduced by NHE. Considering the two parts of the NHE, NHE1 is weaker than NHE2 at lower  
544 horizontal Froude number, but its magnitude grows rapidly as the horizontal Froude number  
545 increases. On the contrary, NHE2 firstly increases but then starts decreasing with the horizontal

546 Froude number, with this change of trend occurring at about  $Fr = 0.48$ . Consequently, NHE1 starts  
547 to be dominant in the reduction of the GWMF above about  $Fr = 0.4$ .

548 For OGWs generated by anisotropic terrain, when the mean flow is perpendicular to the  
549 long axis of the orography ( $\gamma < 1$ ), the GWMF is less reduced than in the isotropic case,  
550 suggesting a weakening of the NHE. This is consistent with the results of OGWs forced by 2D  
551 ridges. Conversely, NHE are enhanced when the mean flow is parallel to the long axis or the  
552 orography ( $\gamma > 1$ ). In the parallel-flow case, the NHE vary by no more than 12.9% with the terrain  
553 anisotropy, and this occurs as the horizontal Froude number tends asymptotically to infinity. Since  
554 this corresponds to a situation in which  $\tau$  approaches zero, the relevance of this effect is even more  
555 limited. When the mean flow is oblique to the main axes of the mountain, NHE exhibit a greater  
556 variation under the joint influence of terrain anisotropy and horizontal wind direction, with a  
557 maximum value twice that of the parallel-flow case. Nevertheless, in either case, it is still the  
558 horizontal Froude number that dominates the variation of the NHE.

559 Given the relatively weak influence of terrain anisotropy and horizontal wind direction on  
560 the NHE, the asymptotic solution of the GWMF for isotropic terrain [i.e., Eq. (21)], which is  
561 simply a function of the horizontal Froude number, may be used to quantify the NHE with a good  
562 accuracy. Benefiting from the analytical form of this expression, the parameterization schemes for  
563 hydrostatic OGWs can be easily extended to nonhydrostatic conditions, which will inevitably  
564 occur in high-resolution NWP and GCMs. It is noteworthy that the horizontal Froude number  
565 depends on the horizontal scale of subgrid-scale orography, which is constrained by the model's  
566 horizontal resolution. Since the NHE are scale-aware (or scale-dependent), they make the  
567 parametrization itself scale-aware. Recently, variable-resolution numerical models have generated  
568 a growing interest (e.g., Skamarock et al. 2012; Davis et al. 2016; Zhou et al. 2019; Zhang et al.

569 2019), as they can significantly reduce the computational costs, while allowing for high-resolution  
 570 modelling in areas of specific interest. A nonhydrostatic parameterization scheme will be  
 571 particularly useful for models with variable-resolution meshes, as it can adjust the parameterized  
 572 GWMF in the fine-resolution regions where NHE are expected to be important, while having little  
 573 influence in the coarse-resolution areas.

574 In our upcoming research, a traditional hydrostatic OGW parameterization scheme will be  
 575 revised taking into account NHE, based on the asymptotic expressions derived in the present study.  
 576 Then the revised scheme will be implemented in a high-resolution numerical model (with a grid  
 577 spacing on the order of 10 km) to investigate the impacts of NHE on the vertical momentum  
 578 transport of subgrid-scale OGWs and their consequences for the large-scale circulation.

579  
 580 *Acknowledgements.* This work is jointly supported by the National Science Foundation of China  
 581 (Grants 41875068, 91837207), the Second Tibetan Plateau Scientific Expedition and Research  
 582 (STEP) program (Grant 2019QZKK0105), and the Beijing Climate Center (QHMS2020002).

583  
 584 **Appendix A: Derivation of the asymptotic pressure perturbation at the surface**

585 According to Eq. (7) in Xu et al. (2017b), for 3D OGWs generated by constant flow over  
 586 an isolated mountain, the polarization relation between the pressure and vertical velocity  
 587 perturbations in spectral space has the simple form:

$$588 \quad \hat{p}(k, l, z) = -i \frac{\bar{\rho}}{K^2} \hat{D} \frac{\partial \hat{w}(z)}{\partial z}. \quad (\text{A1})$$

589 Substitution of Eq. (3) into the above equation yields

$$590 \quad \hat{p}(k, l, z) = i \bar{\rho} \frac{\hat{D}^2}{K^2} m e^{imz} \hat{h}(k, l). \quad (\text{A2})$$

591 Using inverse 2D Fourier transforms, the pressure perturbation in physical space is given by

592 
$$p(x, y, z) = Re \left[ i\bar{\rho} \int_{-\infty}^{\infty} \int_{-\infty}^{\infty} \frac{\bar{D}^2}{K^2} m \hat{h}(k, l) e^{i(kx+ly+mz)} dk dl \right], \quad (A3)$$

593 where  $Re(\cdot)$  denotes the real part of a complex number. For the elliptical bell-shaped mountain  
 594 under consideration, and using polar coordinates for the horizontal wavenumber [see Eq. (8)], the  
 595 pressure perturbation of nonhydrostatic OGWs at  $z = 0$  is

596 
$$p(x, y, 0) = p(S, \Psi, 0) = Re \left[ \frac{i}{\pi} \bar{\rho} N |\tilde{\mathbf{V}}| h_0 \int_0^{\pi} \int_0^{\infty} \frac{\cos(\phi - \chi)}{\sqrt{\cos^2 \phi + \gamma^2 \sin^2 \phi}} \times \right.$$

597 
$$\left. \sqrt{1 - [\tilde{K} Fr \cos(\phi - \chi)]^2} \tilde{K} e^{-\tilde{K}} e^{i\tilde{K} S \cos(\phi - \Psi)} d\tilde{K} d\phi \right], \quad (A4a)$$

598 which can be divided into two parts, i.e.,

599 
$$p_{GW}(S, \Psi, 0) = Re \left[ \frac{i}{\pi} \bar{\rho} N |\tilde{\mathbf{V}}| h_0 \int_0^{\pi} \int_0^{[Fr \cos(\phi - \chi)]^{-1}} \frac{\cos(\phi - \chi)}{\sqrt{\cos^2 \phi + \gamma^2 \sin^2 \phi}} \times \right.$$

600

601 
$$\left. \sqrt{1 - [\tilde{K} Fr \cos(\phi - \chi)]^2} \tilde{K} e^{-\tilde{K}} e^{i\tilde{K} S \cos(\phi - \Psi)} d\tilde{K} d\phi \right]. \quad (A4b)$$

602 
$$p_{evanescent}(S, \Psi, 0) = Re \left[ \frac{i}{\pi} \bar{\rho} N |\tilde{\mathbf{V}}| h_0 \int_0^{\pi} \int_{[Fr \cos(\phi - \chi)]^{-1}}^{\infty} \frac{\cos(\phi - \chi)}{\sqrt{\cos^2 \phi + \gamma^2 \sin^2 \phi}} \times \right.$$

603

604 
$$\left. \sqrt{1 - [\tilde{K} Fr \cos(\phi - \chi)]^2} \tilde{K} e^{-\tilde{K}} e^{i\tilde{K} S \cos(\phi - \Psi)} d\tilde{K} d\phi \right]. \quad (A4c)$$

605 for vertically-propagating OGWs and evanescent waves, respectively. In the deduction of the  
 606 above equations, the following elliptical polar coordinate in physical space was introduced for  
 607 convenience:

608 
$$X = \frac{x}{a} = S \cos \Psi, \quad Y = \frac{y}{b} = S \sin \Psi, \quad (A5)$$

609 where  $S = \frac{1}{a} \sqrt{x^2 + (\gamma y)^2}$  and  $\Psi = \text{atan} \left( \frac{\gamma y}{x} \right)$ .

610 By expanding the vertical wavenumber for small  $Fr$  [see Eq. (13)], the asymptotic surface  
 611 pressure perturbation associated with vertically propagating OGWs can be approximated by the  
 612 sum of  $p_0$ ,  $p_1$  and  $p_2$ , namely,

$$613 \quad p_0(S, \Psi, 0) = Re \left[ \frac{i}{\pi} \bar{\rho} N |\tilde{\mathbf{V}}| h_0 \int_0^\pi \frac{\cos(\phi - \chi)}{\sqrt{\cos^2 \phi + \gamma^2 \sin^2 \phi}} G_0(\phi, S, \Psi) d\phi \right], \quad (\text{A6a})$$

$$614 \quad p_1(S, \Psi, 0) = Re \left[ -\frac{i}{\pi} \bar{\rho} N |\tilde{\mathbf{V}}| h_0 \int_0^\pi \frac{\cos(\phi - \chi)}{\sqrt{\cos^2 \phi + \gamma^2 \sin^2 \phi}} G_1(\phi, S, \Psi) d\phi \right], \quad (\text{A6b})$$

$$615 \quad p_2(S, \Psi, 0) = Re \left[ -\frac{i}{2\pi} Fr^2 \bar{\rho} N |\tilde{\mathbf{V}}| h_0 \int_0^\pi \frac{\cos^3(\phi - \chi)}{\sqrt{\cos^2 \phi + \gamma^2 \sin^2 \phi}} G_2(\phi, S, \Psi) d\phi \right], \quad (\text{A6c})$$

616 with  $G_0$ ,  $G_1$  and  $G_2$  given, respectively, by

$$617 \quad G_0(\phi, S, \Psi) = \int_0^\infty \tilde{K} e^{\tilde{K}[iS\cos(\phi - \Psi) - 1]} d\tilde{K} = Q^{-2}, \quad (\text{A7a})$$

$$618 \quad G_1(\phi, S, \Psi) = \int_{Fr^{-1}}^\infty \tilde{K} e^{\tilde{K}[iS\cos(\phi - \Psi) - 1]} d\tilde{K} = Q^{-2} e^{-QFr^{-1}} (1 + QFr^{-1}), \quad (\text{A7b})$$

$$619 \quad G_2(\phi, S, \Psi) = \int_0^{Fr^{-1}} \tilde{K}^3 e^{\tilde{K}[iS\cos(\phi - \Psi) - 1]} d\tilde{K} \\ 620 \quad = Q^{-4} [6 - e^{-QFr^{-1}} (Q^3 Fr^{-3} + 3Q^2 Fr^{-2} + 6QFr^{-1} + 6)], \quad (\text{A7c})$$

621 and

$$622 \quad Q(\phi, S, \Psi) = 1 - iS\cos(\phi - \Psi) = 1 - i\mu(\phi, S, \Psi). \quad (\text{A8})$$

623 Clearly,  $p_0$  is the pressure perturbation of purely hydrostatic OGWs while  $p_1$  and  $p_2$  are the pressure  
 624 perturbations corresponding to  $\mathbf{\tau}_{asy1}$  and  $\mathbf{\tau}_{asy2}$ .

625 Finally, after some lengthy but straightforward algebraic manipulations, one can obtain the  
 626 three components of the surface pressure perturbation associated with vertically-propagating  
 627 OGWs:

$$628 \quad p_0(S, \Psi, 0) = -\frac{\bar{\rho} N |\tilde{\mathbf{V}}| h_0}{\pi} \int_0^\pi \frac{\cos(\phi - \chi)}{\sqrt{\cos^2 \phi + \gamma^2 \sin^2 \phi}} \frac{2\mu}{(1 + \mu^2)^2} d\phi, \quad (\text{A9a})$$

$$629 \quad p_1(S, \Psi, 0) = \frac{\bar{\rho} N |\tilde{\mathbf{V}}| h_0}{\pi} \int_0^\pi \frac{\cos(\phi - \chi)}{\sqrt{\cos^2 \phi + \gamma^2 \sin^2 \phi}} \frac{1}{(1 + \mu^2)^2} \frac{J_1(\mu) \cos\left(\frac{\mu}{Fr}\right) + J_2(\mu) \sin\left(\frac{\mu}{Fr}\right)}{e^{Fr^{-1}}} d\phi, \quad (\text{A9b})$$

$$630 \quad p_2(S, \Psi, 0) = \frac{\bar{\rho}N|\tilde{V}|h_0}{2\pi} \int_0^\pi \frac{\cos^3(\phi-\chi)}{\sqrt{\cos^2\phi+\gamma^2\sin^2\phi}} \frac{Fr^2}{(1+\mu^2)^4} \left[ J_0(\mu) - \frac{J_3(\mu)\cos\left(\frac{\mu}{Fr}\right) + J_4(\mu)\sin\left(\frac{\mu}{Fr}\right)}{e^{Fr-1}} \right] d\phi, \quad (\text{A9c})$$

631 where

$$632 \quad J_0(\mu) = 24(1 - \mu^2)\mu, \quad (\text{A10a})$$

$$633 \quad J_1(\mu) = \mu \left( 2 + \frac{1+\mu^2}{Fr} \right), \quad (\text{A10b})$$

$$634 \quad J_2(\mu) = 1 - \mu^2 + \frac{1+\mu^2}{Fr}, \quad (\text{A10c})$$

$$635 \quad J_3(\mu) = \mu \left[ 24(1 - \mu^2) - \frac{6(\mu^2-3)(1+\mu^2)}{Fr} + \frac{6(1+\mu^2)^2}{Fr^2} + \frac{(1+\mu^2)^3}{Fr^3} \right], \quad (\text{A10d})$$

$$636 \quad J_4(\mu) = 6(\mu^4 - 6\mu^2 + 1) + \frac{6(1+3\mu^2)(1-\mu^2)}{Fr} + \frac{3(1-\mu^2)(1+\mu^2)^2}{Fr^2} + \frac{(1+\mu^2)^3}{Fr^3}. \quad (\text{A10e})$$

637  
638  
639  
640  
641  
642  
643  
644  
645  
646  
647  
648  
649  
650  
651  
652  
653  
654  
655  
656  
657  
658

## References

Amemiya, A., and K. Sato, 2016: A new gravity wave parameterization including three-dimensional propagation. *J. Meteor. Soc. Japan*, **94**, 237–256, <https://doi.org/10.2151/jmsj.2016-013>

Beljaars, A. C. M., A. R. Brown, and N. Wood, 2004: A new parametrization of turbulent orographic form drag. *Quart. J. Roy. Meteor. Soc.*, **130**, 1327–1347, <https://doi.org/10.1256/qj.03.73>

Broutman, D., J. W. Rottman, and S. D. Eckermann, 2002: Maslov’s method for stationary hydrostatic mountain waves. *Quart. J. Roy. Meteor. Soc.*, **128**, 1159–1171, <https://doi.org/10.1256/003590002320373247>

Broutman, D., J. W. Rottman, and S. D. Eckermann, 2003: A simplified Fourier method for nonhydrostatic mountain waves. *J. Atmos. Sci.*, **60**, 2686–2696, [https://doi.org/10.1175/1520-0469\(2003\)060%3C2686:ASFMFN%3E2.0.CO;2](https://doi.org/10.1175/1520-0469(2003)060%3C2686:ASFMFN%3E2.0.CO;2)

Davis, C. A., D. A. Ahijevych, W. Wang, and W. C. Skamarock, 2016: Evaluating medium-range tropical cyclone forecasts in uniform- and variable-resolution global models. *Mon. Wea. Rev.*, **144**, 4141–4160, <https://doi.org/10.1175/MWR-D-16-0021.1>

Doyle, J. D., and D. R. Durran, 2002: The dynamics of mountain-wave-induced rotors. *J. Atmos. Sci.*, **59**, 186–201, [https://doi.org/10.1175/1520-0469\(2002\)059%3C0186:TDOMWI%3E2.0.CO;2](https://doi.org/10.1175/1520-0469(2002)059%3C0186:TDOMWI%3E2.0.CO;2)

Eckermann, S. D., J. Ma, and D. Broutman, 2015: Effects of horizontal geometrical spreading on the parameterization of orographic gravity wave drag. Part I: Numerical transform solutions. *J. Atmos. Sci.*, **72**, 2330–2347, <https://doi.org/10.1175/JAS-D-14-0147.1>

659 Ehard, B., and Coauthors, 2017: Vertical propagation of large-amplitude mountain waves in the  
660 vicinity of the polar night jet. *J. Geophys. Res. Atmos.*, **122**, 1423–1436,  
661 <https://doi.org/10.1002/2016JD025621>

662 Fritts, D. C., and M. J. Alexander, 2003: Gravity wave dynamics and effects in the middle  
663 atmosphere. *Rev. Geophys.*, **41**, 1003, <https://doi.org/10.1029/2001RG000106>

664 Grubišić, V., and P. K. Smolarkiewicz, 1997: The effect of critical levels on 3D orographic flows:  
665 Linear regime. *J. Atmos. Sci.*, **54**, 1943–1960. [https://doi.org/10.1175/1520-  
666 0469\(1997\)054<1943:TEOCLO>2.0.CO;2](https://doi.org/10.1175/1520-0469(1997)054<1943:TEOCLO>2.0.CO;2)

667 Guarino, M.-V., and M. A. C. Teixeira, 2017: Non-hydrostatic effects on mountain wave breaking  
668 in directional shear flows. *Quart. J. Roy. Meteor. Soc.*, **143**, 3291–3297.  
669 <https://doi.org/10.1002/qj.3157>

670 Kim, Y.-J., and A. Arakawa, 1995: Improvement of orographic gravity wave parameterization  
671 using a mesoscale gravity wave model. *J. Atmos. Sci.*, **52**, 1875–  
672 1902, [https://doi.org/10.1175/1520-0469\(1995\)052%3C1875:IOOGWP%3E2.0.CO;2](https://doi.org/10.1175/1520-0469(1995)052%3C1875:IOOGWP%3E2.0.CO;2)

673 Kim, Y. -J., and J. D. Doyle, 2005: Extension of an orographic-drag parameterization scheme to  
674 incorporate orographic anisotropy and flow blocking. *Quart. J. Roy. Meteor. Soc.*, **131**,  
675 1893–1921, <https://doi.org/10.1256/qj.04.160>

676 Kim, Y. -J., S. D. Eckermann, and H. Y. Chun, 2003: An overview of the past, present and future  
677 of gravity-wave drag parametrization for numerical climate and weather prediction models.  
678 *Atmos.– Ocean*, **41**, 65–98, <https://doi.org/10.3137/ao.410105>

679 Klemp, J. B., and D. R. Durran, 1983: An upper boundary condition permitting internal gravity  
680 wave radiation in numerical mesoscale models. *Mon. Wea. Rev.*, **111**, 430–444,  
681 [https://doi.org/10.1175/1520-0493\(1983\)111%3C0430:AUBCPI%3E2.0.CO;2](https://doi.org/10.1175/1520-0493(1983)111%3C0430:AUBCPI%3E2.0.CO;2)

682 Lott, F., and M. Miller, 1997: A new sub-grid orographic drag parameterization: Its formulation  
683 and testing. *Quart. J. Roy. Meteor. Soc.*, **123**, 101–127,  
684 <https://doi.org/10.1002/qj.49712353704>.

685 Marks, C. J., and S. D. Eckermann, 1995: A three-dimensional nonhydrostatic ray-tracing model  
686 for gravity waves: Formulation and preliminary results for the Middle atmosphere. *J.*  
687 *Atmos. Sci.*, **52**, 1959–1984, [https://doi.org/10.1175/1520-](https://doi.org/10.1175/1520-0469(1995)052%3C1959:ATDNRT%3E2.0.CO;2)  
688 [0469\(1995\)052%3C1959:ATDNRT%3E2.0.CO;2](https://doi.org/10.1175/1520-0469(1995)052%3C1959:ATDNRT%3E2.0.CO;2)

689 McFarlane, N. A., 1987: The effect of orographically excited gravity wave drag on the general  
690 circulation of the lower stratosphere and troposphere. *J. Atmos. Sci.*, **44**, 1775–  
691 1800, [https://doi.org/10.1175/1520-0469\(1987\)044<1775:teooeg>2.0.co;2](https://doi.org/10.1175/1520-0469(1987)044<1775:teooeg>2.0.co;2)

692 Miranda, P. M. A., and I. N. James, 1992: Non-linear three-dimensional effects on the wave drag:  
693 Splitting flow and breaking waves. *Quart. J. Roy. Meteor. Soc.*, **118**, 1057–1081.  
694 <https://doi.org/10.1002/qj.49711850803>

695 Palmer, T. N., G. J. Shutts, and R. Swinbank, 1986: Alleviation of systematic westerly bias in  
696 general circulation and numerical weather prediction models through an orographic gravity  
697 wave drag parameterization. *Quart. J. Roy. Meteor. Soc.*, **112**, 1001–1039,  
698 <https://doi.org/10.1002/qj.49711247406>

699 Phillips, D. S., 1984: Analytical surface pressure and drag for linear hydrostatic flow over three-  
700 dimensional elliptical mountains. *J. Atmos. Sci.*, **41**, 1073–1084,  
701 [https://doi.org/10.1175/1520-0469\(1984\)041%3C1073:ASPADF%3E2.0.CO;2](https://doi.org/10.1175/1520-0469(1984)041%3C1073:ASPADF%3E2.0.CO;2)

702 Plougonven R., A. de la Cámara, A. Hertzog., and F. Lott, 2020: How does knowledge of  
703 atmospheric gravity waves guide their parameterizations? *Quart. J. Roy. Meteor. Soc.*, **146**,  
704 1529–1543, <https://doi.org/10.1002/qj.3732>

705 Pulido, M., and C. Rodas, 2011: A higher-order ray approximation applied to orographic waves:  
706 Gaussian beam approximation. *J. Atmos. Sci.*, **68**, 46–60,  
707 <https://doi.org/10.1175/2010JAS3468.1>

708 Scinocca, J. F., and N. A. McFarlane, 2000: The parametrization of drag induced by stratified flow  
709 over anisotropic orography. *Quart. J. Roy. Meteor. Soc.*, **126**, 2353–2393,  
710 <https://doi.org/10.1002/qj.49712656802>

711 Scorer, R. S., 1949: Theory of waves in the lee of mountains. *Quart. J. Roy. Meteor. Soc.*, **75**, 41–  
712 56, <https://doi.org/10.1002/qj.49707532308>

713 Shutts, G., 1995: Gravity-wave drag parameterization over complex terrain: The effect of critical-  
714 level absorption in directional wind-shear. *Quart. J. Roy. Meteor. Soc.*, **121**, 1005–1021,  
715 <https://doi.org/10.1002/qj.49712152504>

716 Shutts, G. J., 1998: Stationary gravity-wave structure in flows with directional wind shear. *Quart.*  
717 *J. Roy. Meteor. Soc.*, **124**, 1421–1442, <https://doi.org/10.1002/qj.49712454905>

718 Skamarock, W., J. B. Klemp, M. G. Duda, and coauthors, 2012: A multiscale nonhydrostatic  
719 atmospheric model using centroidal voronoi tessellations and C-grid staggering. *Mon. Wea.*  
720 *Rev.*, **140**, 3090–3105, <https://doi.org/10.1175/MWR-D-11-00215.1>

721 Smith, R. B., 1979: The influence of mountains on the atmosphere. *Advances in Geophysics*, **21**,  
722 87–230, [https://doi.org/10.1016/S0065-2687\(08\)60262-9](https://doi.org/10.1016/S0065-2687(08)60262-9)

723 Smith, R. B., 1980. Linear theory of stratified flow past an isolated mountain. *Tellus*, **32**, 348–364.  
724 <https://doi.org/10.1111/j.2153-3490.1980.tb00962.x>

725 Smith, R. B., 1985: On severe downslope winds. *J. Atmos. Sci.*, **42**, 2597–2603,  
726 [https://doi.org/10.1175/1520-0469\(1985\)042%3C2597:OSDW%3E2.0.CO;2](https://doi.org/10.1175/1520-0469(1985)042%3C2597:OSDW%3E2.0.CO;2)

727 Song, I.-S., and H.-Y. Chun, 2008: A Lagrangian spectral parameterization of gravity wave drag  
728 induced by cumulus convection. *J. Atmos. Sci.*, **65**, 1204–1224,  
729 <https://doi.org/10.1175/2007JAS2369.1>

730 Teixeira, M. A. C., and P. M. A. Miranda, 2006: A linear model of gravity wave drag for  
731 hydrostatic sheared flow over elliptical mountains. *Quart. J. Roy. Meteor. Soc.*, **132**, 2439–  
732 2458. <https://doi.org/10.1256/qj.05.220>

733 Teixeira, M. A. C., and P. M. A. Miranda, 2009: On the momentum fluxes associated with  
734 mountain waves in directionally sheared flows. *J. Atmos. Sci.*, **66**, 3419–3433.  
735 <https://doi.org/10.1175/2009JAS3065.1>

736 Teixeira, M. A. C., and C. L. Yu, 2014: The gravity wave momentum flux in hydrostatic flow with  
737 directional shear over elliptical mountains. *Eur. J. Mech. Fluids*, **47B**, 16–31,  
738 <https://doi.org/10.1016/j.euromechflu.2014.02.004>.

739 Teixeira, M. A. C., P. M. A. Miranda, and R. M. Cardoso, 2008: Asymptotic gravity wave drag  
740 expression for non-hydrostatic rotating flow over a ridge. *Quart. J. Roy. Meteor.*  
741 *Soc.*, **134**, 271–276. <https://doi.org/10.1002/qj.196>

742 Teixeira, M. A. C., P. M. A., Miranda, and M. A. Valente, 2004. An analytical model of mountain  
743 wave drag for wind profiles with shear and curvature. *J. Atmos. Sci.*, **61**, 1040–1054.  
744 [https://doi.org/10.1175/1520-0469\(2004\)061<1040:AAMOMW>2.0.CO;2](https://doi.org/10.1175/1520-0469(2004)061<1040:AAMOMW>2.0.CO;2)

745 Turner, H. V., M. A. C. Teixeira, J. Methven, and S. B. Vosper, 2019: Sensitivity of the surface  
746 orographic gravity wave drag to vertical wind shear over Antarctica. *Quart. J. Roy. Meteor.*  
747 *Soc.*, **145**, 164-178. <https://doi.org/10.1002/qj.3416>

748 Wurtele, M. G., R. D. Sharman, and A. Datta, 1996: Atmospheric lee waves. *Ann. Rev. Fluid*  
749 *Mech.*, **28**, 429–476, <https://doi.org/10.1146/annurev.fl.28.010196.002241>

750 Xu, X., Y. Wang, and M. Xue, 2012: Momentum flux and flux divergence of gravity waves in  
751 directional shear flows over three-dimensional mountains. *J. Atmos. Sci.*, **69**, 3733–3744,  
752 <https://doi.org/10.1175/JAS-D-12-044.1>

753 Xu, X., J. Song, Y. Wang, and M. Xue, 2017a: Quantifying the effect of horizontal propagation of  
754 three-dimensional mountain waves on the wave momentum flux using Gaussian Beam  
755 Approximation. *J. Atmos. Sci.*, **74**, 1783–1798, <https://doi.org/10.1175/JAS-D-16-0275.1>

756 Xu, X., S. Shu, and Y. Wang, 2017b: Another look on the structure of mountain waves: A spectral  
757 perspective. *Atmos. Res.*, **191**, 156–163, <https://doi.org/10.1016/j.atmosres.2017.03.015>

758 Xu, X., Y. Tang, Y. Wang, and M. Xue, 2018: Directional absorption of mountain waves and its  
759 influence on the wave momentum transport in the Northern Hemisphere. *J. Geophys. Res.*  
760 *Atmos.*, **123**, 2640-2654, <https://doi.org/10.1002/2017JD027968>

761 Xu, X., M. Xue, M. A. C. Teixeira, J. Tang, and Y. Wang, 2019: Parameterization of directional  
762 absorption of orographic gravity waves and its impact on the atmospheric general

763           circulation simulated by the Weather Research and Forecasting model. *J. Atmos. Sci.*, **76**,  
764           3435–3453. <https://doi.org/10.1175/JAS-D-18-0365.1>

765    Xu, X., M. A. C. Teixeira, M. Xue, Y. Lu, and J. Tang, 2020: Impacts of wind profile shear and  
766           curvature on the parameterized orographic gravity wave stress in the Weather Research  
767           and Forecasting model. *Q. J. R. Meteorol. Soc.*, **146**, 3086-3100.  
768           <https://doi.org/10.1002/qj.3828>

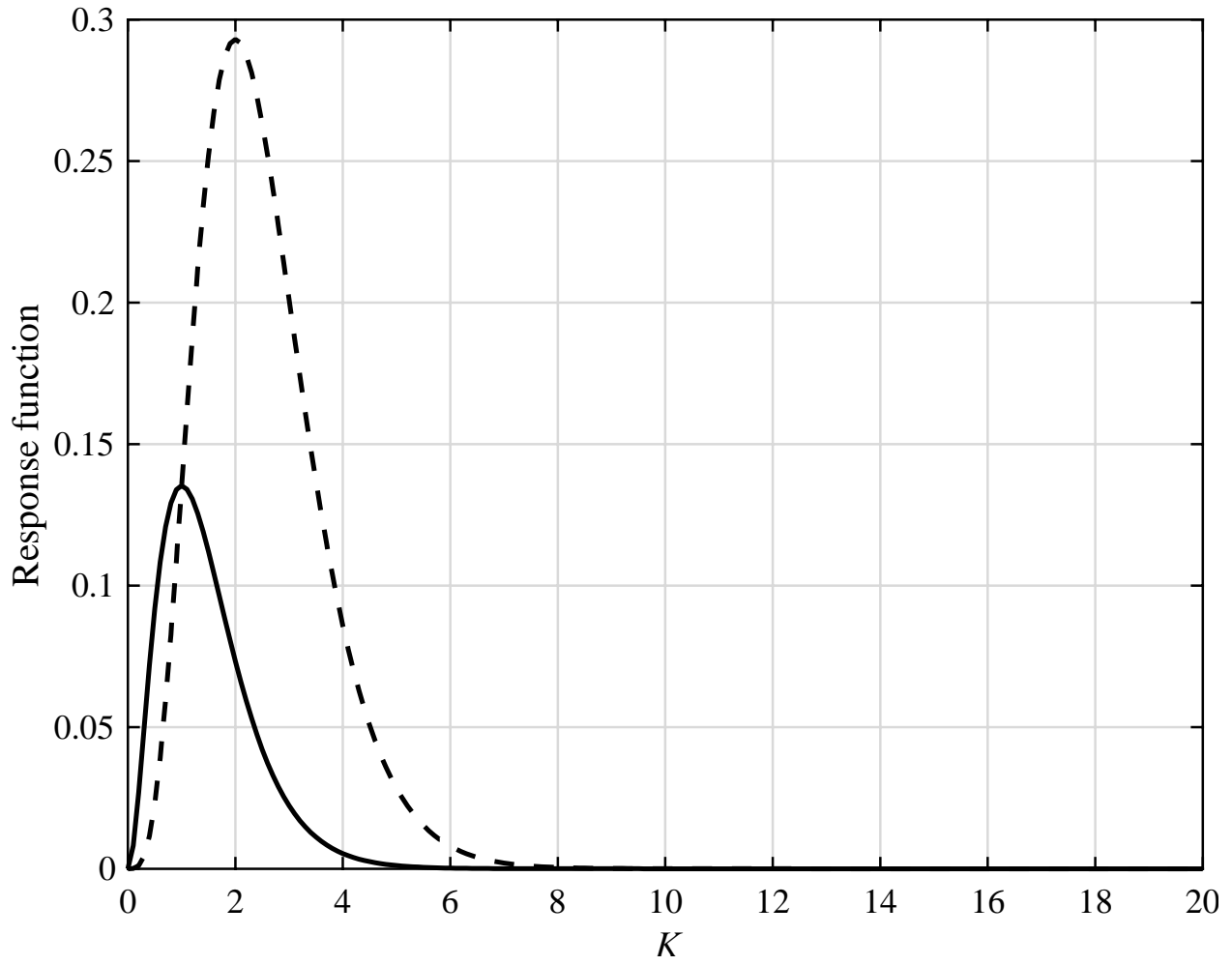
769    Xue, M., and A. J. Thorpe, 1991: A mesoscale numerical model using the nonhydrostatic sigma-  
770           coordinate equations: Model experiments with dry mountain flows. *Mon. Wea. Rev.*, **119**,  
771           1168–1185, [https://doi.org/10.1175/1520-  
772           0493\(1991\)119%3C1168:AMNMUT%3E2.0.CO;2](https://doi.org/10.1175/1520-0493(1991)119%3C1168:AMNMUT%3E2.0.CO;2)

773    Xue, M., K. K. Droegemeier, and V. Wong, 2000: The Advanced Regional Prediction System  
774           (ARPS) – A multi-scale nonhydrostatic atmospheric simulation and prediction model. Part  
775           I: Model dynamics and verification. *Meteorol. Atmos. Phys.*, **75**, 161–193

776    Zängl, G., 2003: Orographic gravity waves close to the nonhydrostatic limit of vertical propagation.  
777           *J. Atmos. Sci.*, **60**, 2045–2063, [https://doi.org/10.1175/1520-  
778           0469\(2003\)060%3C2045:OGWCTT%3E2.0.CO;2](https://doi.org/10.1175/1520-0469(2003)060%3C2045:OGWCTT%3E2.0.CO;2)

779    Zhang, Y., J. Li, R. Yu, and coauthors, 2019: A layer-averaged nonhydrostatic dynamical  
780           framework on an unstructured mesh for global and regional atmospheric modeling: Model  
781           description, baseline evaluation, and sensitivity exploration. *J. Adv. Model. Earth Sy.*, **11**,  
782           1685–1714, <https://doi.org/10.1002/2017MS001088>

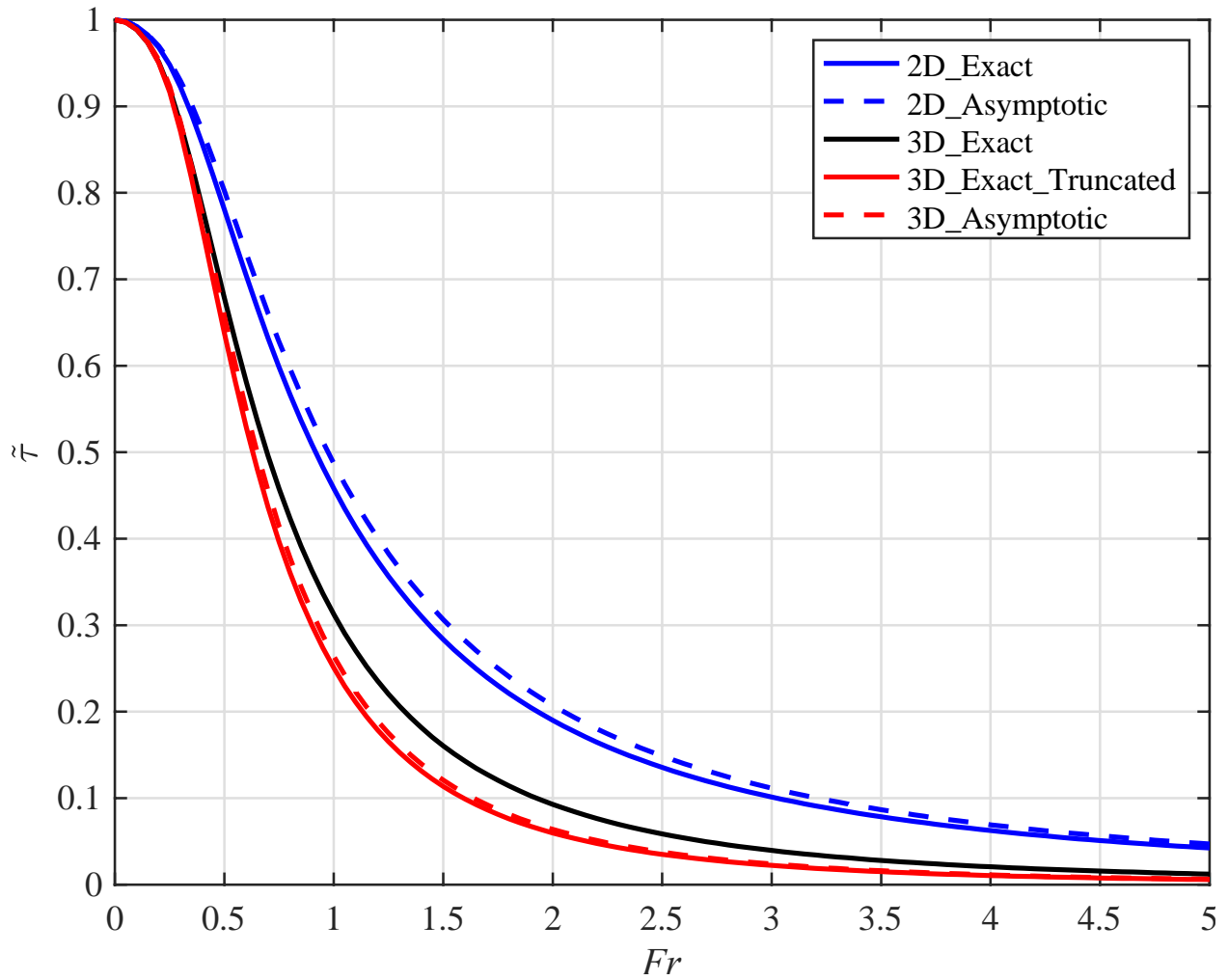
783 Zhou, L., S.-J. Lin, J.-H. Chen, and coauthors, 2019: Toward convective-scale prediction within  
784 the next generation global prediction system. *Bull. Amer. Meteor. Soc.*, 100, 1225–1243,  
785 <https://doi.org/10.1175/BAMS-D-17-0246.1>



786

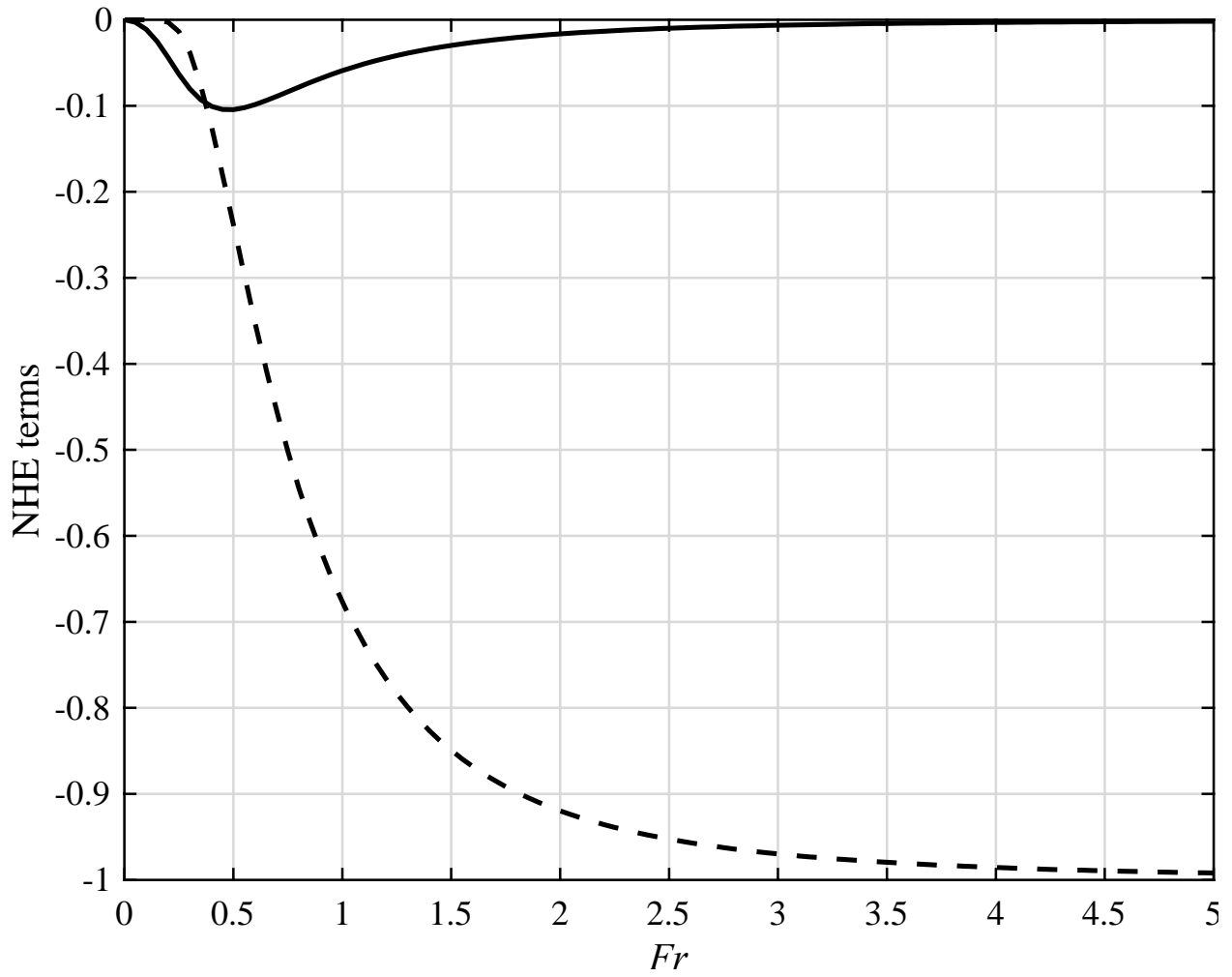
787 Fig. 1 Response functions  $\tilde{K}^2 e^{-2\tilde{K}}$  (solid) and  $\tilde{K}^4 e^{-2\tilde{K}}$  (dashed).

788



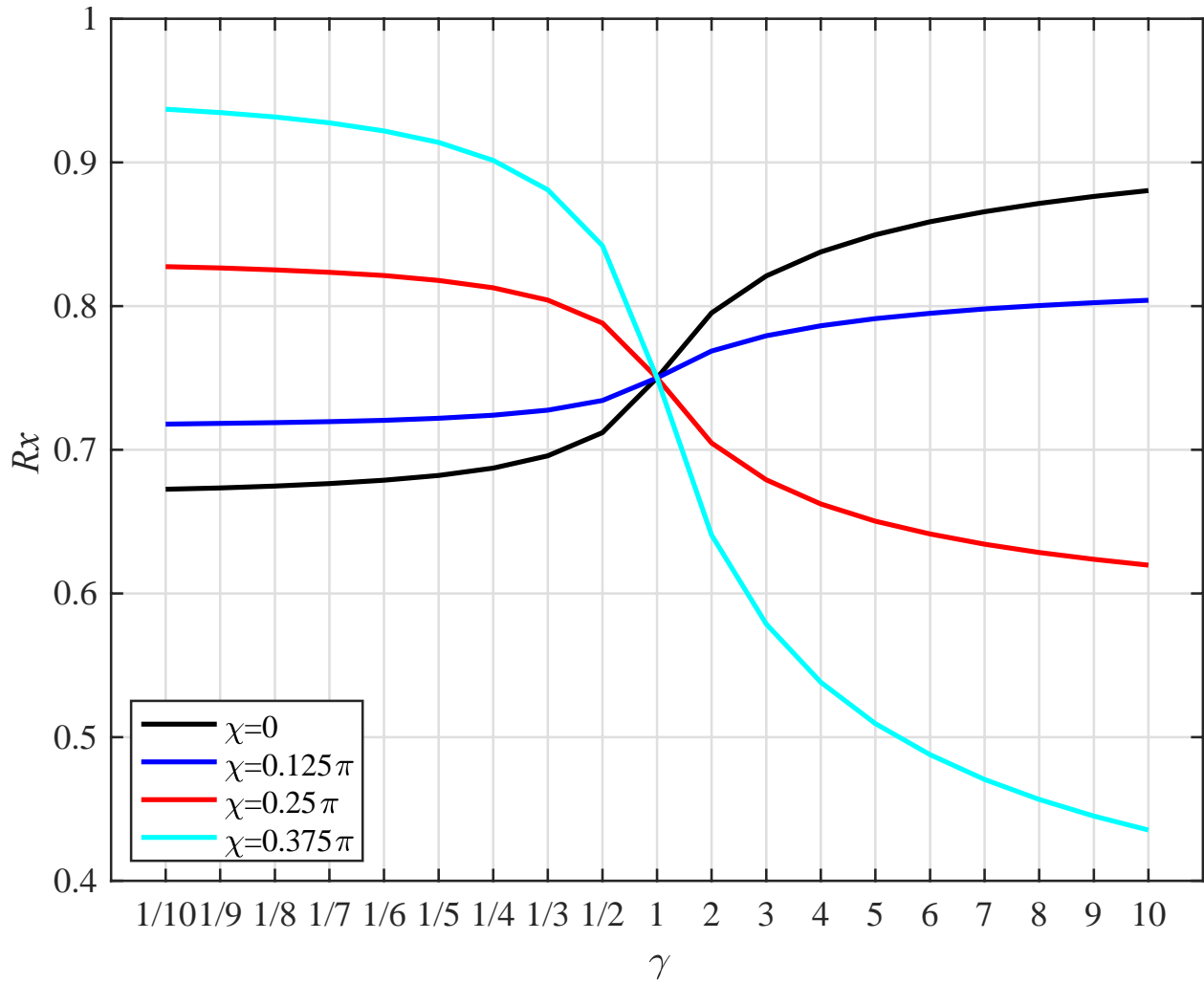
789

790 Fig. 2 Variation of the normalized GWMF ( $\tilde{\tau}$ ) with the horizontal Froude number ( $Fr$ ). Blue lines  
 791 are for the nonhydrostatic OGWs forced by 2D bell-shaped ridges, while the black and red lines  
 792 are for those forced by 3D circular bell-shaped mountains. The normalization is made with respect  
 793 to their hydrostatic counterparts.



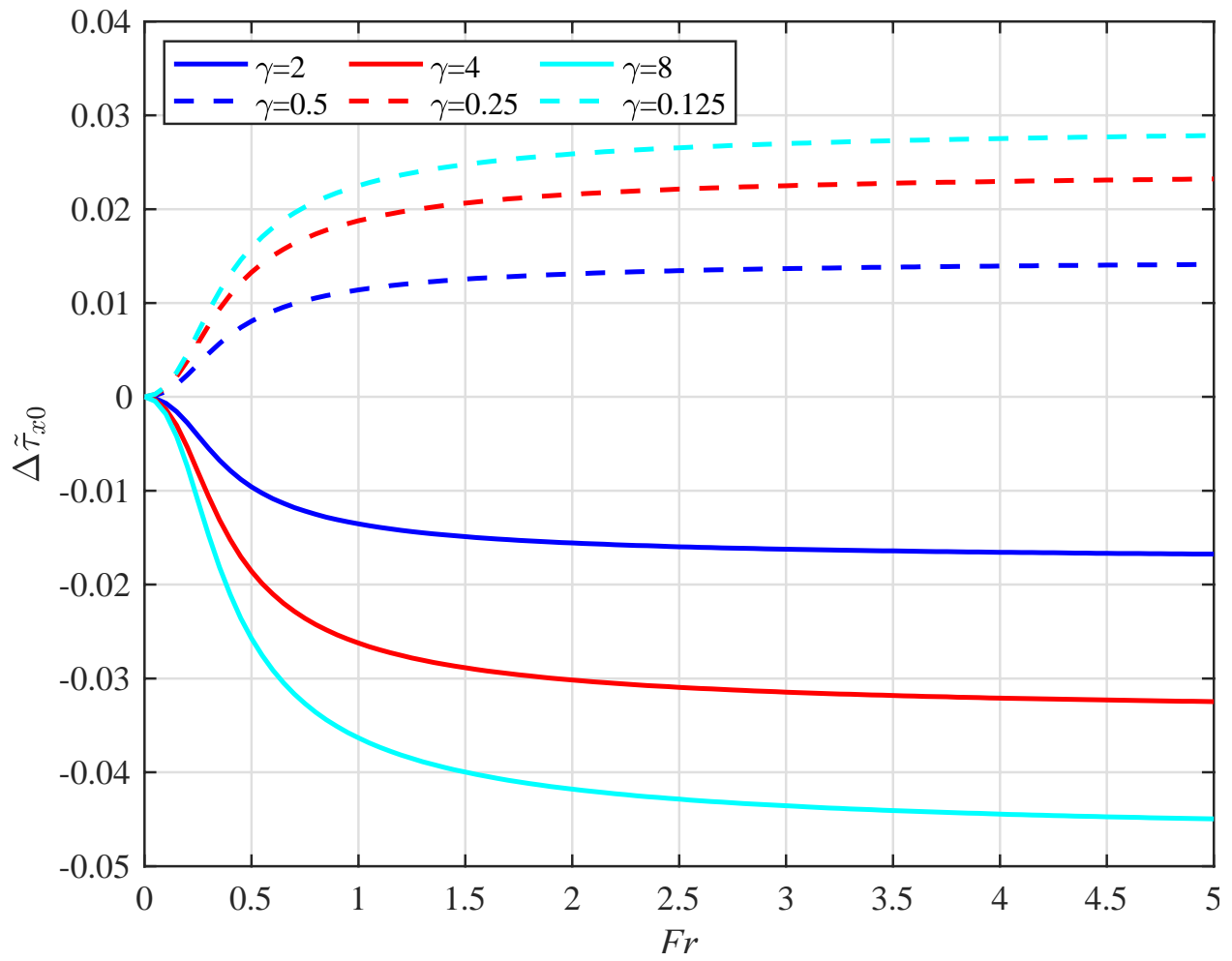
794

795 Fig. 3 Variations of the NHE1 (dashed) and NHE2 (solid) terms with the horizontal Froude number  
 796 ( $Fr$ ) in the case of isotropic terrain.



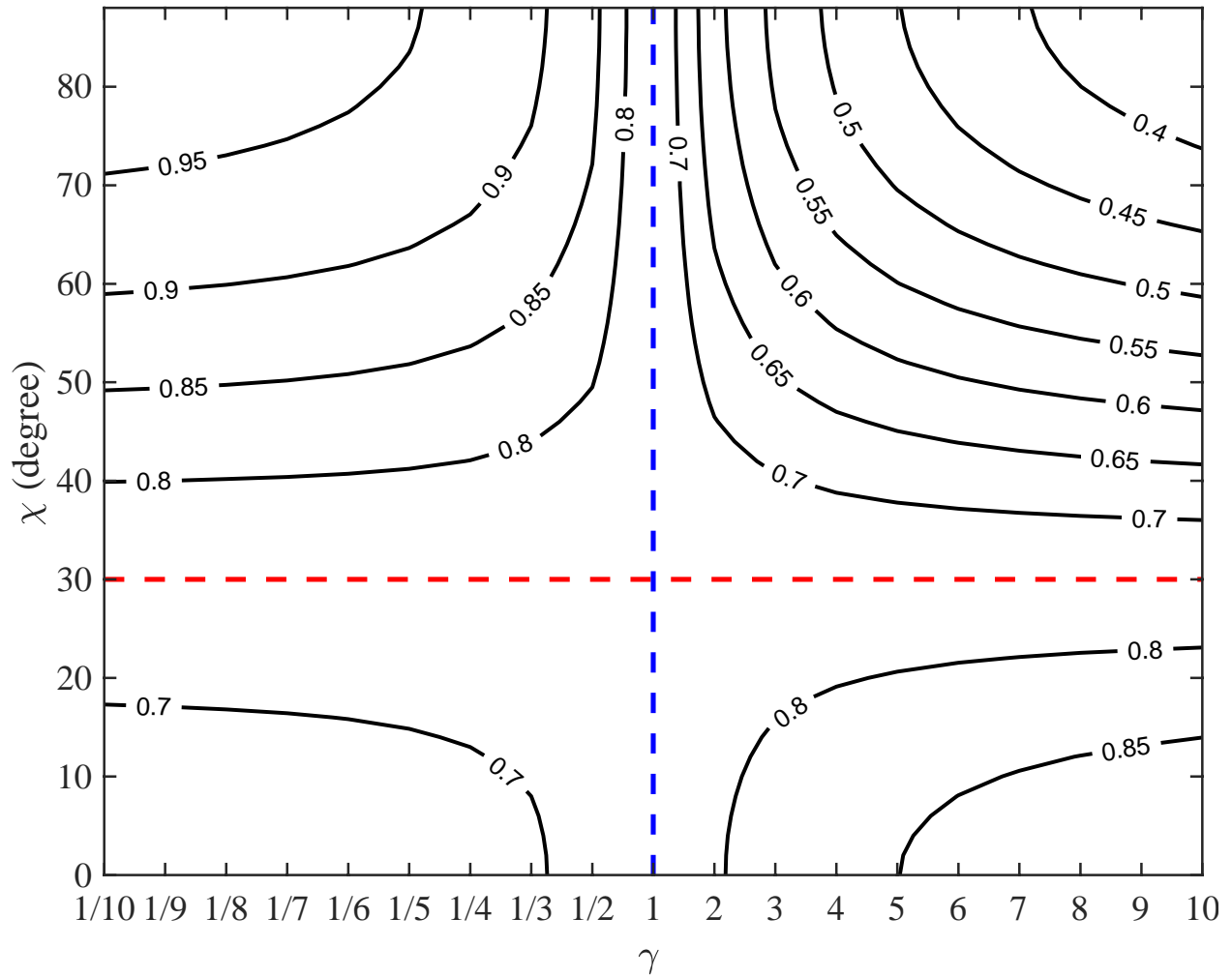
797

798 Fig. 4 Variation of  $R_x(\gamma, \chi)$  as a function of terrain anisotropy ( $\gamma$ ) for different horizontal wind  
 799 directions ( $\chi$ ).

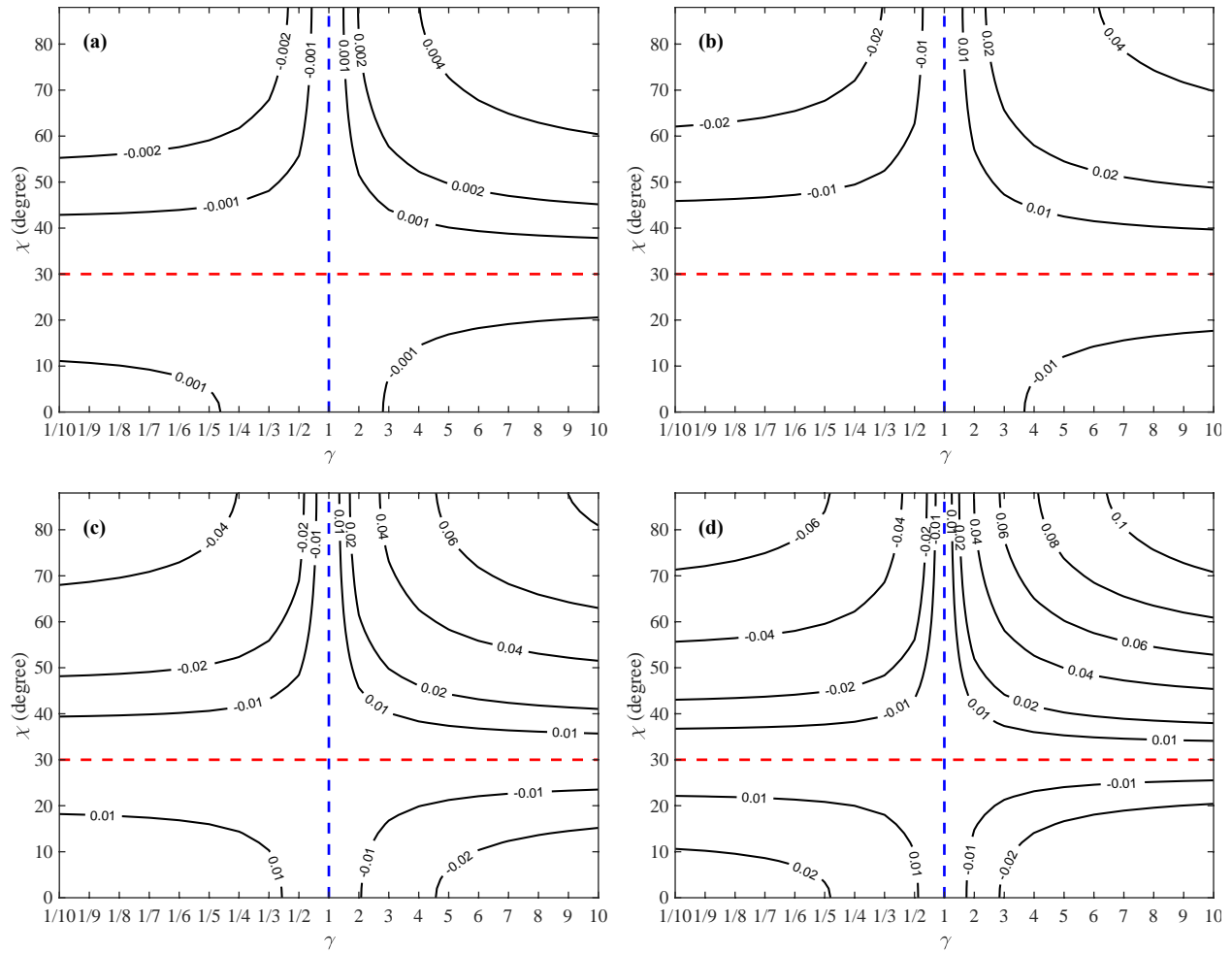


800

801 Fig. 5 Variation of  $\Delta\tilde{\tau}_{x0}$  in the parallel-flow case as a function of horizontal Froude number ( $Fr$ )  
 802 for different terrain anisotropies ( $\gamma$ ).

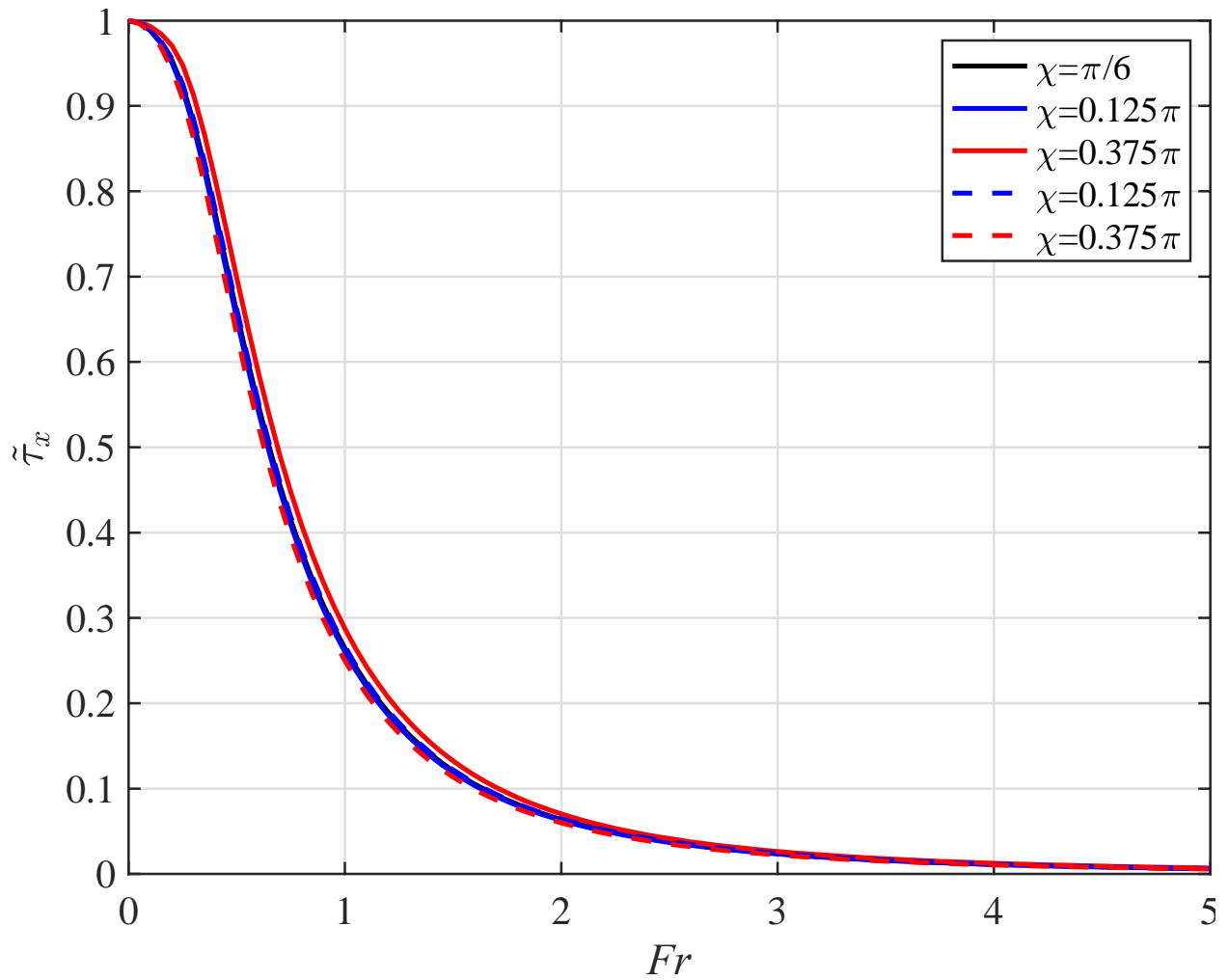


803  
 804 Fig. 6 Distribution of  $R_x(\gamma, \chi)$  in  $\gamma$ - $\chi$  parameter space. The red line represents  $\chi = \frac{\pi}{6}$  while the  
 805 blue line indicates  $\gamma = 1$ .



806

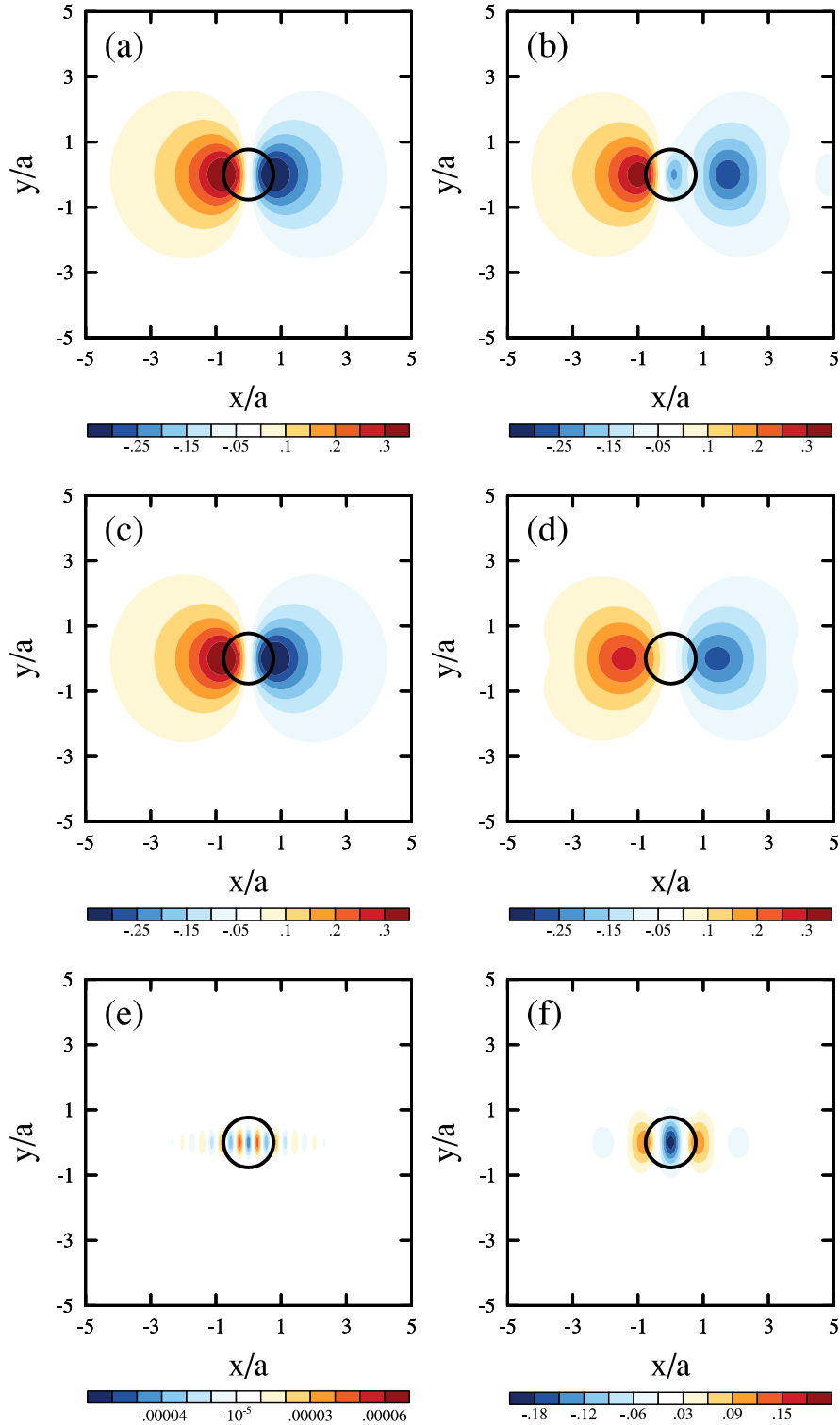
807 Fig. 7 Distribution of  $\Delta\tilde{\tau}_x$  in  $\gamma$ - $\chi$  parameter space at different horizontal Froude numbers: (a)  $Fr$   
 808  $= 0.1$ , (b)  $Fr = 0.3$ , (c)  $Fr = 0.5$ , and (d)  $Fr = 1.0$ . The red line represents  $\chi = \frac{\pi}{6}$  while the blue line  
 809 indicates  $\gamma = 1$ .



810

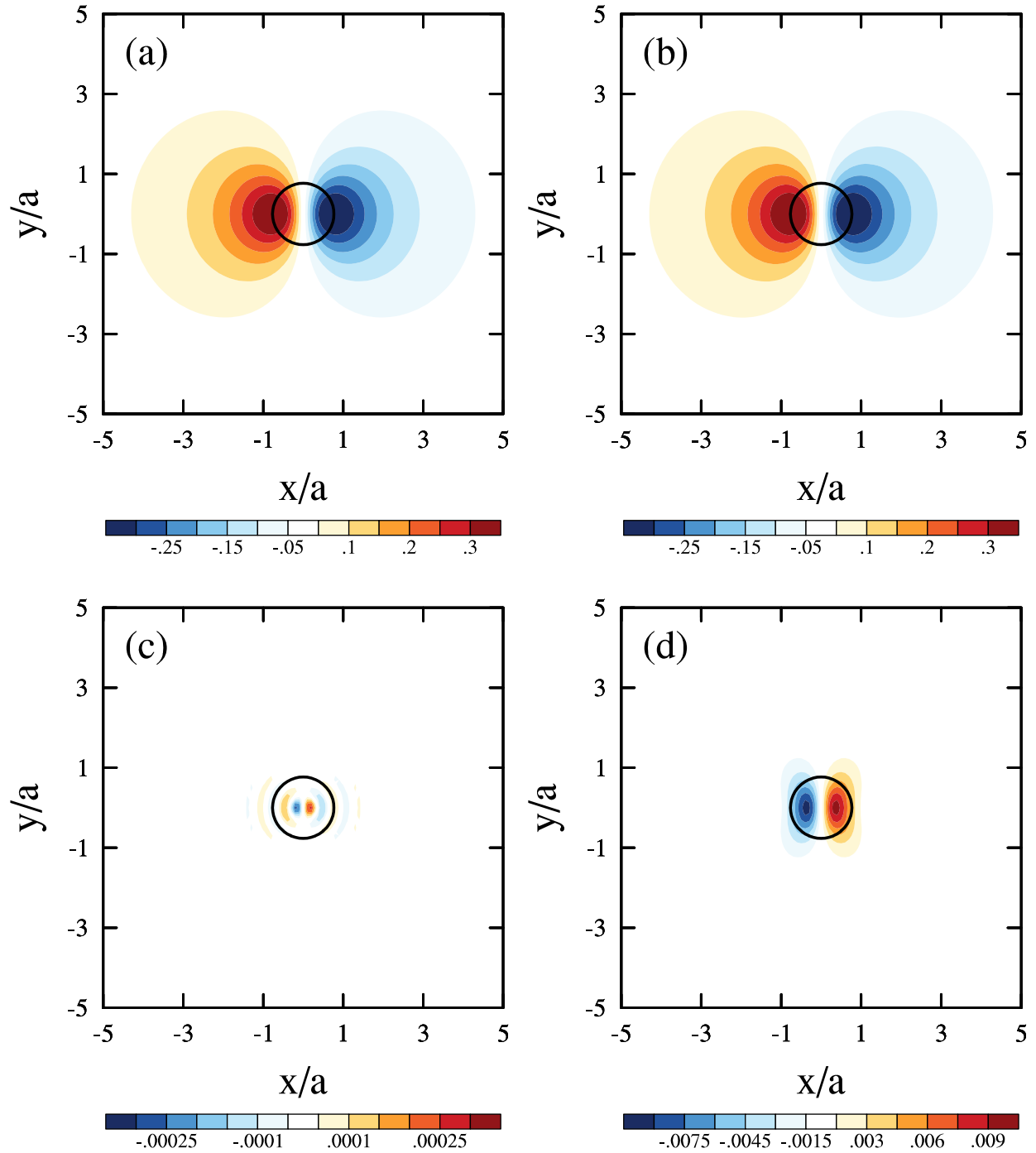
811 Fig. 8 Variation of the  $x$ -component of the normalized GWMF ( $\tilde{\tau}_x$ ) in the oblique-flow case as a  
 812 function of the horizontal Froude number ( $Fr$ ). Solid and dashed lines are for  $\gamma = 8$  and  $\gamma = \frac{1}{8}$ ,  
 813 respectively.

814



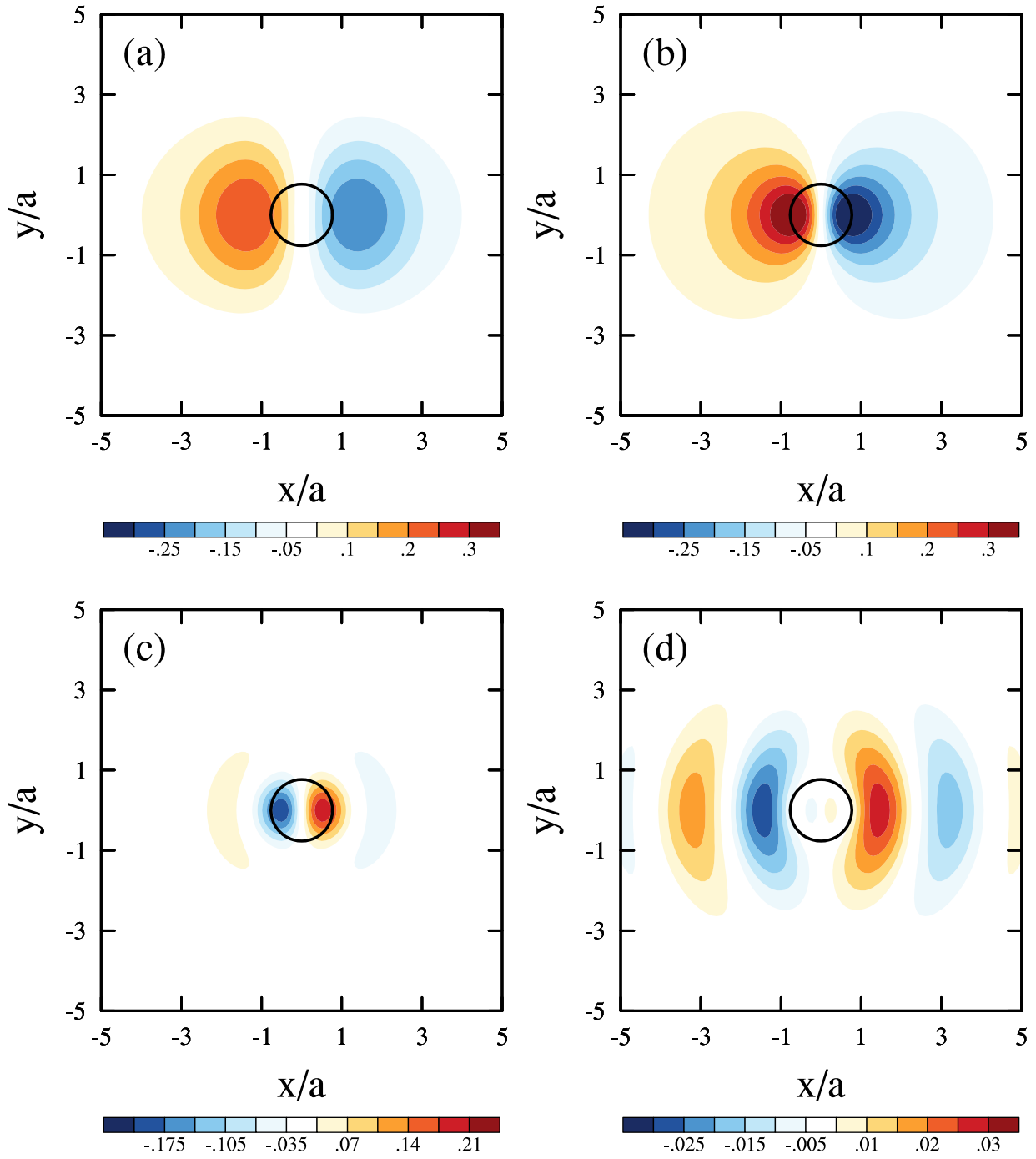
815  
816  
817  
818  
819  
820

Fig. 9 Exact surface pressure perturbation (top) of nonhydrostatic OGWs forced by a circular bell-shaped mountain, which is the sum of  $p_{GW}$  (middle) and  $p_{evanescent}$  (bottom). See appendix for details. (a) (c) and (e) are for  $Fr = 0.1$ , while (b) (d) and (f) are for  $Fr = 0.5$ . The pressure perturbations are scaled with  $\bar{\rho}N|\tilde{V}|h_0$ . The axes are scaled by the mountain half width  $a$ . The black circle indicates the contour of  $0.5 h_0$ , with  $h_0$  being the maximum elevation of the mountain.



821

822 Fig. 10 (a) Asymptotic surface pressure perturbation of nonhydrostatic vertically propagating  
 823 OGWs forced by a circular bell-shaped mountain at  $Fr = 0.1$ , which is the sum of (b)  $p_0$ , (c)  $p_1$  and  
 824 (d)  $p_2$  (see appendix for details). The pressure perturbations are scaled with  $\bar{\rho}N|\tilde{\mathbf{V}}|h_0$ . The axes are  
 825 scaled by the mountain half width  $a$ . The black circle indicates the contour  $0.5 h_0$ , with  $h_0$  being  
 826 the maximum elevation of the mountain.



827

828 Fig. 11 Same as Fig. 10 but for  $Fr = 0.5$ .